Accepted manuscript. Published in International Journal of Damage Mechanics (2022). Version of record: https://doi.org/10.1177/10567895221095890. This is the authors' final version after peer review. Please cite the published article.

A directional microcrack damage theory for brittle solids based on continuous hyperplasticity

International Journal of Damage Mechanics
XX(X):2–31
©The Author(s) 2021
Reprints and permission:
sagepub.co.uk/journalsPermissions.nav
DOI: 10.1177/ToBeAssigned
www.sagepub.com/
SAGE

Mitul Sisodiya[1] and Yida Zhang[2]

Abstract

We present a novel microcrack-damage theory for brittle solids under compression. Instead of using internal variables like zeroth, second or fourth rank damage tensors, the state of material damage is represented by an internal function that encapsulates the information of direction, density and size of microcracks. Just like other internal variables, the evolution of this state function must obey the second law of thermodynamics for arbitrary loading paths. This is done by casting the model in the framework of continuous hyperplasticity and enforcing a non-negative dissipation rate functional. The proposed framework offers predictions on the continuous evolution of microcrack density and the induced material anisotropy along with the macroscopic stress-strain curves. The use of continuous damage function grants the model significantly enhanced resolution in characterizing the direction-dependent response of cracked solids compared to classical models that are based on damage tensors. Two scenarios are considered in developing the theory, one assumes frictionless cracks and the other incorporates friction between crack surfaces. The results highlight that inelasticity, pressure dependence, and loading-unloading hysteresis exhibited by brittle solids are natural consequences of frictional microcracks. The proposed theory offers a generic and versatile framework to upscale micromechanical processes operating at individual crack scale to explain the macroscopic behavior of cracked solids.

Keywords

Anisotropic damage, Continuous hyperplasticity, Frictional microcracks, Crack distribution density, Hysteresis

Prepared using sagej.cls *[Version: 2017/01/17 v1.20]*

Introduction

The nonlinear, anisotropic, hysteretic, and pressure-dependent behaviors of brittle solids such as rocks and concrete are tightly related to the pre-existing microcracks as well as the nucleation and the growth of microcracks upon loading Walsh (1965); Horii and Nemat-Nasser (1983); David et al. (2012); Ashby and Sammis (1990). A wide spectrum of formulations has been developed to model the mechanical response of cracked brittle solids, ranging from fracture mechanics-based discontinuous models (Horii et al. 1986; Carol et al. 1997; Kachanov 1993; Paliwal and Ramesh 2008; Sammis and Ashby 1986) to damage mechanics-based continuum models (Fanella and Krajcinovic 1988; Yazdani and Schreyer 1988; Cicekli et al. 2007; Zhu et al. 2009; Kachanov 1958). While the discontinuous models offer significant insights on the onset and evolution of post-rupture behaviors (Horii et al. 1986), their analytical solutions may be only obtained for highly simplified geometries and crack arrangements (Kachanov 1993). Continuum damage mechanics on the other hand skips the details about the size, location, and orientation of individual microcracks via a smeared damage variable and focuses on their effects on the macroscopic representative element volume (REV) (Krajcinovic 1996; Lemaitre 2012). This treatment enables the development of tangible constitutive models for brittle solids that may be coupled with other inelastic and multiphysical processes such as plasticity (Al-Rub and Voyiadjis 2003; Einav et al. 2007), viscoplasticity (Børvik et al. 2001), healing (Voyiadjis et al. 2011; Zhu and Arson 2015), and environmental dependencies (Bui et al. 2017; Pense et al. 2016).

Due to the planar nature of microcracks, their presence introduces strong anisotropy on the mechanical properties of the REV (Chau and Wong 1997). The state of damage is therefore often represented by second/fourth order damage tensors or sets of scalar damage parameters to preserve the directional data of microcracks during upscaling and to capture the resultant stiffness and strength anisotropy. Various approaches have been used to relate the stiffness degradation of cracked solid to the damage variables. Phenomenological models often use the concept of strain equivalence to map the stress in the cracked material to a fictitious uncracked material through a damage tensor that can be second rank (Voyiadjis et al. 2008) or fourth rank (Ju 1989). These models can be also cast in terms of damage-dependent free energy functions (Shao and Rudnicki 2000; Zhu and Arson 2014). On the other hand,

[1,2]Civil, Environmental and Architectural Engineering, University of Colorado Boulder, CO 80309-0428, USA

Corresponding author:
Yida Zhang,Civil, Environmental and Architectural Engineering, University of Colorado Boulder, CO 80309-0428, USA.
Email: yida.zhang@colorado.edu

Prepared using sagej.cls

micromechanical models treat cracks as inclusions with vanishingly small aspect ratio by which the change in compliance/stiffness of the material can be derived (Kachanov 1982; Ju 1991; Zhu et al. 2009; Bikong et al. 2015). Continuum damage models can then be developed through homogenization via noninteracting scheme (Kachanov 1982; Fanella and Krajcinovic 1988) or self-consistent schemes (Sumarac and Krajcinovic 1987; Ju 1991). More recently, damage models based on the higher order homogenization scheme of Castañeda and Willis (1995) (PCW) have been developed (Zhu et al. 2009; Bikong et al. 2015; Zhu and Shao 2016). However, the basic noninteracting scheme remains relevant for offering simple explicit expressions for compliance/stiffness change subjected to microcracking. Kachanov (1993) showed that the noninteracting method remains accurate for non-vanishing crack density, provided that the mutual positions of cracks are random, due to the cancellation of the competing interaction effects of shielding and amplifications.

Despite the wide usage of tensorial damage variables in above models, it is important to note that they are still approximations of the crack distribution density of the material. Such approximation has following limitations: 1) sophisticated microcrack distribution patterns due to complex loading history (e.g. rocks near geological faults) (Hoxha et al. 2005) cannot be represented by these approximations; 2) mapping a damage tensor back to a crack distribution may yield regions that have negative crack density which is apparently not physical (Lubarda and Krajcinovic 1993). For these reasons, the spatial and directional resolution of the predicted material anisotropy is significantly compromised. A possible remediation is to look at a finite number of discrete planes and examine the local stress-strain relation or damage evolution along those planes such as in microplane models (Bažant and Prat 1988; Ožbolt and Bažant 1992) and microcrack models (Zhu and Shao 2016; Jin and Arson 2017). A continuous representation of the directional statistics of microcracks, however, is still lacking. From a practical standpoint, enhanced representation of microcrack distribution is of particular importance in engineering critical geological structures (e.g. underground nuclear waste repositories) where the in-situ geomaterials are characterized by multiple sets of microcracks originated by the bedding plane and the lithostatic stress history. Excavation and construction will induce new microcrack groups that can further complicate the crack distribution density and the resultant anisotropic mechanical and hydraulic properties (Pardoen et al. 2016; Tsang et al. 2012).

The purpose of this study is therefore to develop a continuum damage theory that allows high-resolution description and modeling of the direction-dependent mechanical behaviors of brittle solids. The idea is to introduce continuum crack distribution density as a fundamental internal state function instead of its discrete approximation or the traditional scalar/tensorial damage variables. The initial distribution represents the inherent microcracks in the solid, while its evolution collectively reflects the initiation, growth and coalescence of the cracks in the microscale. To comply with thermodynamic constraints under arbitrary loading paths, the theory will be cast in the continuous hyperplasticity

formalism (Houlsby and Puzrin 2007) where a non-negative dissipation rate functional is enforced. While the hyperplasticity framework has been successfully applied to the field of continuum damage mechanics (Einav et al. 2007; Nguyen and Houlsby 2008; Arson 2020), the present work is one of the first to employ the continuous hyperplasticity to incorporate a internal state function. In the following, we start by revisiting the elasticity of damaged solids with many noninteracting frictionless cracks (section 'Compliance of microcracked solid'). Continuous hyperplasticity is introduced and adopted to obtain the evolution laws for the damage distribution function (section 'Continuous hyperplasticity'). The formulation is then extended to include friction at crack surfaces (section 'Incorporation of crack friction'). Finally, the theory is applied to capture the stress-strain behavior of various brittle rocks observed in biaxial experiments (section 'Application of the directional damage model'). This study focuses on the compressive response of microcracked solid, which is the dominating loading situation for most geomaterials. The development is also limited to two-dimensional (2D) plane-strain condition to focus our attention more on the underlying physics and micromechanics. Paths towards its three-dimensional (3D) generalization and other future extensions are discussed at the end (section 'Conclusions').

Compliance of microcracked solid

The change of compliance due to microcracking under compressive stress is studied in this section using the noninteracting homogenization scheme. While the interaction effects become significant near the peak of stress-strain curve where the directional distribution of microcracks becomes highly localized and the cracks are about to coalesce. We have ignored the interaction effects in this first study for the sake of simplicity. Higher order interaction schemes such as the PCW scheme by Castañeda and Willis (1995) may be incorporated to account for microcrack interactions in future generalizations (Zhu et al. 2009; Zhu and Shao 2016). The REV is treated as a linear elastic matrix containing single or multiple microcracks.

Single microcrack

The energy and compliance change of a REV induced by a single penny shaped microcrack is given by Budiansky and O'connell (1976); Chau and Wong (1997). Here a similar procedure is followed to derive the compliance change due to a line crack closed under compression in 2D plane strain condition

$$\Delta C^1_{ijkl} = \frac{\pi\,(\kappa+1)}{16\mu}\frac{a^2}{A}\beta_{ijkl}, \tag{1}$$

where the free indices $i, j, k, l \in \{1, 2\}$; ΔC^1_{ijkl} is the change in secant compliance with the superscript '1' denoting single crack; a is the half size of the crack; μ the shear modulus of the uncracked matrix; A the area of the 2D REV; $\kappa = 3 - 4\nu$ with ν being the Poisson's ratio of the uncracked matrix; β_{ijkl} is a fourth order tensor solely dependent on the orientation of the crack. It is assumed that the size of the REV is much larger than the size of the microcracks so that $A \gg (2a)^2$. For a closed crack under compressive far-field stresses

$$\beta_{ijkl} = n_i n_k \delta_{jl} + n_j n_k \delta_{il} + n_i n_l \delta_{jk} + n_j n_l \delta_{ik} - 4 n_i n_j n_k n_l, \tag{2}$$

where n_i is the crack normal vector; δ_{ij} is the Kronecker delta. For convenience, the material parameters in equation (1) can be collected in a single constant

$$b = \frac{\pi (\kappa + 1)}{16 \mu}. \tag{3}$$

Assuming the crack does not propagate and using equations (1)-(3), the total form of the stress-strain relationship of the REV can be written as

$$\varepsilon_{ij} = C^0_{ijkl}\sigma_{kl} + \Delta C^1_{ijkl}\sigma_{kl} = C^0_{ijkl}\sigma_{kl} + b\frac{a^2}{A}\beta_{ijkl}\sigma_{kl}, \tag{4}$$

where ε_{ij} is the strain; σ_{kl} is the stress and C^0_{ijkl} is the compliance of the intact matrix. It is possible to show that the fourth order tensor β_{ijkl} (equation (2)) can be decomposed as dyads of two second order tensors through some algebraic rearrangement:

$$\beta_{ijkl} = \xi_{ij}\xi_{kl} \quad \text{with} \quad [\xi] = \begin{bmatrix} 2n_1 n_2 & n_2^2 - n_1^2 \\ n_2^2 - n_1^2 & -2n_1 n_2 \end{bmatrix}. \tag{5}$$

The second order tensor ξ_{ij} can be physically interpreted by considering a local coordinate system aligned with the microcrack face, as demonstrated in Figure 1. The basis of the global coordinates is denoted by $\mathbb{E}\{\mathbf{e}_1, \mathbf{e}_2\}$. For every microcrack, a local coordinate system with basis $\mathbb{E}\prime\{\hat{\mathbf{e}}\prime_1, \hat{\mathbf{e}}\prime_2\}$ is defined such that $\hat{\mathbf{e}}\prime_2 = \mathbf{n}$ is normal and $\hat{\mathbf{e}}\prime_1$ is parallel to the crack surface. The basis $\mathbb{E}$ and $\mathbb{E}\prime$ are related through the rotation tensor Q_{ij}.

$$[Q] = \begin{bmatrix} n_2 & n_1 \\ -n_1 & n_2 \end{bmatrix} = \begin{bmatrix} cos(\omega) & -sin(\omega) \\ sin(\omega) & cos(\omega) \end{bmatrix}. \tag{6}$$

Thus, the shear stress component in frame $\mathbb{E}\prime$ is obtained as

$$\tau\prime = \sigma\prime_{12} = \sigma\prime_{21} = Q_{i1}Q_{j2}\sigma_{ij} = Q_{i2}Q_{j1}\sigma_{ij}, \tag{7}$$

and ξ_{ij} can be expressed as following by substituting the component of Q_{ij}:

$$\xi_{ij} = Q_{i1}Q_{j2} + Q_{i2}Q_{j1}. \tag{8}$$

By observing equations (7) and (8), it is readily apparent that ξ_{ij} maps the stress components in the global frame to the shear stress in the local frame::

$$\tau\prime = \sigma\prime_{12} = Q_{i1}Q_{j2}\sigma_{ij} = \frac{1}{2}\xi_{ij}\sigma_{ij}. \tag{9}$$

The stress-strain relationship can be rewritten by substituting equations (5) and (9) into equation (4):

$$\varepsilon_{ij} = C^0_{ijkl}\sigma_{kl} + 2b\frac{a^2}{A}\xi_{ij}\tau\prime. \tag{10}$$

The corresponding energy potential is obtained by integrating equation (10) with respect to stress and taking the energy at stress-free reference state as zero:

$$g^1\left(\sigma_{ij}, \omega, a\right) = -\frac{1}{2}C^0_{ijkl}\sigma_{ij}\sigma_{kl} - 2b\tau\prime^2\,\frac{a^2}{A}, \tag{11}$$

where g^1 is the Gibbs free energy of the REV containing a single microcrack of size $2a$ and orientation ω with respect to the global coordinate system. The first term on the right hand side (RHS) is the Gibbs free energy of the intact matrix, free of any internal discontinuities. The second term on the RHS represents change of Gibbs free energy caused by the microcrack.

Multiple microcracks

Let us consider a REV with N noninteracting microcracks embedded in the solid matrix as shown in Figure 2. Each microcrack is characterized by orientation $\omega \in [0\,,\,\pi]$ and half-size $a \in [0\,,\,a_{max}]$. Therefore, the microcracks in the REV can be represented through a distribution density function $\hat{\rho}(\omega, a)$ that satisfies

$$\int_0^{\pi}\int_0^{a_{max}} \hat{\rho}(\omega, a)\, da\, d\omega = 1. \tag{12}$$

The number of microcracks dN oriented between ω to $\omega + d\omega$ and with size between a to $a + da$ is thus given by

$$dN = N\hat{\rho}(\omega, a)\, da\, d\omega. \tag{13}$$

Under the noninteracting assumption, the energy change of the REV due to multiple cracks can be obtained by summing up the contribution of each microcrack. In the limiting case of continuous

distribution, this summation is replaced by an integration over the orientation ω and size a, giving the total Gibbs energy of the REV

$$g[\sigma_{ij}, \hat{\rho}(\omega, a), N] = -\frac{1}{2} C^0_{ijkl}\sigma_{ij}\sigma_{kl} - \int_0^{\pi} 2b\tau\prime^2 \left(\int_0^{a_{max}} \frac{N}{A} a^2 \hat{\rho}(\omega, a)\, da \right) d\omega. \tag{14}$$

The second term on the RHS of equation (14) encapsulates all the effects caused by microcracking on the REV. Specifically, the inner integral contains the effect of crack size a and the crack density N/A on the extent of the damage along direction ω, and the outer integral collects such effect along all orientations. To focus the current study on the direction-dependent damage and the induced material anisotropy, we smear the effect of crack size and density and define the inner integral as the *directional damage*:

$$\hat{d}(\omega) = \int_0^{a_{max}} \frac{N}{A} a^2 \hat{\rho}(\omega, a)\, da, \tag{15}$$

where the superposed '`hat`' on $\hat{d}$ is to highlight its dependency on orientation. It will be similarly used to denote other direction-dependent internal state functions in the remainder of this paper. Substituting equation (15) into equation (14) gives the final form of Gibbs free energy for multi-crack system

$$g[\sigma_{ij}, \hat{d}] = -\frac{1}{2} C^0_{ijkl}\sigma_{ij}\sigma_{kl} - \int_0^{\pi} 2b\tau\prime^2 \hat{d}\, d\omega. \tag{16}$$

The stress-strain relation can be derived from (16) via the hyperelastic relation:

$$\varepsilon_{ij} = -\frac{\partial g}{\partial \sigma_{ij}} = C^0_{ijkl}\sigma_{kl} + 2b \int_0^{\pi} \xi_{ij}\tau\prime \hat{d}\, d\omega. \tag{17}$$

Continuous hyperplasticity

The above discussion focuses on the compliance and the energy potential of a microcracked solid with fixed crack size and density (i.e. the non-evolving scenario). This section tackles the evolution problem by permitting $\hat{d}$ to evolve with external loading. To ensure consistency with the second law of thermodynamics, such evolution law is developed in the framework of continuous hyperplasticity (Puzrin and Houlsby 2001b,a; Houlsby and Puzrin 2007) which is an extension of the hyperplasticity theory (Collins and Houlsby 1997). In this framework, the constitutive behavior of an inelastic material is completely determined by two scalar functions, namely the free energy potential that defines elasticity and the non-negative dissipation rate function that describes the inelastic flow. The state of the material is typically represented by scalar or tensorial state variables appearing in the two functions. However in our case, the state of damage is instead characterized by a continuous internal state function $\hat{d}(\omega)$ over

$[0\,,\,\pi]$ subjected to evolution. Therefore, the free energy and the dissipation rate become functions of functions (i.e. functionals) for which the continuous hyperplasticity framework is suitable. Note that the above derivation is based on mode II crack opening displacement only, assuming that all the cracks are closed under compression.

Formulation

Continuous hyperplasticity extends the hyperplasticity formalism to include internal state functions in the free energy and the dissipation rate functionals as detailed in Houlsby and Puzrin (2007); Einav and Puzrin (2004). Here we keep our derivation concise by specifying the only internal state function as the directional damage defined in equation (15). Take the isothermal work equation as the starting point

$$\dot{W} = \dot{\psi} + \phi, \tag{18}$$

where $\dot{W} = \sigma_{ij}\dot{\varepsilon}_{ij}$ is the rate of work input, ψ is the Helmholtz free energy, and ϕ is the dissipation rate function. g is related to ψ through a Legendre transform with respect to strain:

$$g = \psi - \sigma_{ij}\varepsilon_{ij}. \tag{19}$$

Combining equation (18) and equation (19) yields the work equation in terms of g:

$$\dot{g} + \dot{\sigma}_{ij}\varepsilon_{ij} + \phi = 0. \tag{20}$$

The Gibbs free energy for multi-cracked system (equation 16) consists of two terms. The first term is a function of stress and the second term is a functional of $\hat{d}$. Thus equation (16) can be rewritten in a more familiar form as in the literature (Puzrin and Houlsby 2001b; Houlsby and Puzrin 2007):

$$g[\sigma_{ij}, \hat{d}] = g_1(\sigma_{ij}) + \int_0^\pi \hat{g}_2(\sigma_{ij}, \hat{d}, \omega)\, d\omega \quad \text{with} \tag{21}$$

$$g_1(\sigma_{ij}) = -\frac{1}{2}C^0_{ijkl}\sigma_{ij}\sigma_{kl}, \quad \hat{g}_2(\sigma_{ij}, \hat{d}, \omega) = -2b\tau\prime^2\hat{d}. \tag{22}$$

The rate of change of g can be derived from equation (21) as:

$$\dot{g} = \dot{g}[\sigma_{ij}, \hat{d}, \dot{\sigma}_{ij}, \dot{\hat{d}}] = \left(\frac{\mathrm{d}g_1}{\mathrm{d}\sigma_{ij}} + \int_0^\pi \frac{\partial \hat{g}_2}{\partial \sigma_{ij}}\, d\omega\right)\dot{\sigma}_{ij} - \int_0^\pi \hat{\chi}_d\dot{\hat{d}}\, d\omega, \tag{23}$$

where we denote $\hat{\chi}_d = -\partial \hat{g}_2 / \partial \hat{d}$ as the thermodynamic conjugate of damage or the *damage stress*:

$$\hat{\chi}_d = 2b\tau\prime^2. \tag{24}$$

As stated before, the second law requires a non-negative overall dissipation rate ϕ throughout any deformation process. Here we require a more strict condition such that, during damaging, the microcracks in every direction have a non-negative contribution to the overall dissipation. Implicit to this assumption is that the energy dissipation along each direction is independent of its adjacent directions, making the current model a "local" one in the directional sense. As a result, the model currently ignores the possible kinking effect (i.e. change of direction during propagation) which is required to generate wing cracks. This is consistent with the previous mode-II crack opening assumption in developing the elastic matrices. Such assumption permits this study to focus on establishing the basic thermodynamic structure of the directional damage model with simplest form of evolution laws. This constraint may be relaxed in the future by introducing directionally coupled dissipation functionals inspired by the mechanics of wing cracks (Horii et al. 1986) and implemented using the algorithm proposed by Jin and Arson (2018). Mimicking the expression of g and considering noninteracting cracks, the following dissipation functional is proposed as

$$\phi = \int_0^\pi \hat{\phi}\, d\omega \qquad \text{with} \quad \hat{\phi}(\omega, \dot{\hat{d}}) \geq 0, \quad \forall \omega \in [0\ \pi]. \tag{25}$$

For rate-independent processes considered in the current study, the dissipation has to be first-order homogeneous in $\dot{\hat{d}}$ (Puzrin and Houlsby 2001b). Thus equation (25) can be written as follows according to Euler's theorem

$$\phi = \int_0^\pi \frac{\partial \hat{\phi}}{\partial \dot{\hat{d}}} \dot{\hat{d}}\, d\omega = \int_0^\pi \hat{\tilde{\chi}}_d \dot{\hat{d}}\, d\omega \geq 0, \tag{26}$$

where $\hat{\tilde{\chi}}_d = \partial \dot{\hat{\phi}} / \partial \dot{\hat{d}}$ denotes the damage stress conjugates to the rate of damage, which can be called the *dissipative damage stress* to not confuse with $\hat{\chi}_d$. Substituting equations (23) and (26) into equation (20) gives:

$$\left(\varepsilon_{ij} + \frac{\partial g}{\partial \sigma_{ij}} \right) \dot{\sigma}_{ij} + \int_0^\pi \left(\hat{\chi}_d - \hat{\tilde{\chi}}_d \right) \dot{\hat{d}}\, d\omega = 0. \tag{27}$$

equation (27) must hold true for arbitrary stress and damage increments. Thus the first term leads to the usual hyperelastic relation used in deriving equation (17):

$$\varepsilon_{ij} = -\frac{\partial g}{\partial \sigma_{ij}} = -\frac{\mathrm{d} g_1}{\mathrm{d} \sigma_{ij}} - \int_0^\pi \frac{\partial \hat{g}_2}{\partial \sigma_{ij}}\, d\omega. \tag{28}$$

The second term of equation (27) implies $\hat{\chi}_d = \hat{\bar{\chi}}_d$ which is one form of Ziegler's orthogonality condition (Houlsby 2014). In the ideal case of frictionless cracks, energy can only be dissipated through the initiation and growth of microcracks. Therefore, we propose a simple linear relation between the directional dissipation rate and the damage rate as

$$\hat{\phi} = \hat{\kappa}|\dot{\hat{d}}|, \tag{29}$$

where $\hat{\kappa}$ is a non-negative hardening parameter related to $\hat{d}$. The damage yield function $\hat{\bar{y}}_d$ can be obtained via degenerated Legendre transformation of $\hat{\phi}$:

$$\hat{\bar{y}}_d\left(\hat{\bar{\chi}}_d, \hat{\kappa}\right) = \hat{\bar{\chi}}_d^2 - \hat{\kappa}^2 \leq 0 \quad \text{or} \quad \hat{y}_d\left(\hat{\chi}_d, \hat{\kappa}\right) = \hat{\chi}_d^2 - \hat{\kappa}^2 \leq 0, \tag{30}$$

where $\hat{\bar{y}}_d$ and $\hat{y}_d$ are yield function in dissipative and true stresses, respectively. It is clear now that $\hat{\kappa}$ serves as the threshold damage stress that characterizes the onset of damage. Note that $\hat{y}_d$ and $\hat{\kappa}$ are both functions of direction and therefore the yield condition should be checked for every direction upon loading/unloading. Yielding in a given direction implies the growth of damage and hence microcracking along that direction. In response to an arbitrary external loading, cracks along some orientations will propagate while others remain stationary, in agreement with experimental observations. It is therefore necessary to define the set of directions where damage evolution is activated and the yielding and consistency conditions are enforced:

$$\Theta^d = \{\omega \in [0, \pi] \quad | \quad \hat{y}_d = 0 \text{ and } \dot{\hat{y}}_d = 0\}. \tag{31}$$

Substituting equation (30) and using equation (31), the flow rule or in this case the damage evolution law can be written as

$$\dot{\hat{d}} = \hat{\lambda}_d \frac{\partial \hat{\bar{y}}_d}{\partial \hat{\bar{\chi}}_d} = \begin{cases} 2\hat{\lambda}_d \hat{\bar{\chi}}_d & \text{for}\, \omega \in \Theta^d, \\ 0 & \text{otherwise.} \end{cases} \tag{32}$$

The rate form of $\hat{y}_d$ in equation (30) gives the consistency condition

$$\hat{\chi}_d \dot{\hat{\chi}}_d - \hat{\kappa} \frac{\partial \hat{\kappa}}{\partial \hat{d}} \dot{\hat{d}} = 0 \qquad \text{for}\, \omega \in \Theta^d. \tag{33}$$

By substituting equation (32) into equation (33) and setting $\hat{\chi}_d = \hat{\bar{\chi}}_d$, one obtains

$$\hat{\lambda}_d = \frac{\dot{\hat{\chi}}_d}{2\hat{\chi}_d} \left(\frac{\partial \hat{\kappa}}{\partial \hat{d}}\right)^{-1} = \frac{\dot{\hat{\chi}}_d}{2\hat{\kappa}} \left(\frac{\partial \hat{\kappa}}{\partial \hat{d}}\right)^{-1} \qquad \text{for}\, \omega \in \Theta^d. \tag{34}$$

The damage evolution law can be finally expressed by substituting equation (34) into equation (32):

$$\dot{\hat{d}} = \begin{cases} \dot{\hat{\chi}}_d \left(\frac{\partial \hat{\kappa}}{\partial \hat{d}}\right)^{-1} & \text{for } \omega \in \Theta^d, \\ 0 & \text{otherwise}, \end{cases} \tag{35}$$

where $\partial\hat{\kappa}/\partial\hat{d}$ controls the rate of damage growth and is determined by the function $\hat{\kappa}(\hat{d})$. Finally, the incremental constitutive relation for frictionless microcrack model can be derived by differentiating equation (17) with respect to time and eliminating $\dot{\hat{d}}$ via equation (35):

$$\dot{\varepsilon}_{ij} = C^0_{ijkl}\dot{\sigma}_{kl} + 2b\int_0^{\pi} \xi_{ij}\dot{\tau}\prime\hat{d}\, d\omega + 2b\int_{\Theta^d} \xi_{ij}\tau\prime\dot{\hat{\chi}}_d \left(\frac{\partial\hat{\kappa}}{\partial\hat{d}}\right)^{-1} d\omega. \tag{36}$$

Model response

Let us examine the key features of the model in plane strain uniaxial loading by assuming a simple linear $\hat{\kappa}(\hat{d})$ relation (i.e. $\partial\hat{\kappa}/\partial\hat{d} =$ constant). The parameters used are listed in Table 1.

The initial damage is set as zero and the initial threshold damage stress κ_0 is set as $50kPa$ for all directions to represent an initially intact and isotropic material (Figure 4-I). A uniaxial compression test is conducted along the vertical direction and the predicted stress-strain response is shown in Figure 3. It is observed that the predicted curve follows the intact material compliance till the onset of damage. During the elastic stage, the damage stress $\hat{\chi}_d$ starts to grow anisotropically within the REV. At point 'II', $\hat{\chi}_d$ in a few directions becomes equal to $\hat{\kappa}_0$ and thus the yield condition is satisfied (Figure 4-II). The damage is observed to first initiate at an angle of $45°$ to the loading direction, indicating that only microcracks oriented along those directions start to grow at point 'II' in Figure 3. This prediction is a consequence of assuming frictionless crack surfaces. It is also noted that for all other orientations, the yield condition is not satisfied and therefore no damage evolution. Upon further loading, the response becomes nonlinear due to a combination of enlarged damage orientations and more damage accumulation along the previously yielded orientations. In the yielded zones, $\hat{\kappa}$ evolves together with $\hat{\chi}_d$ to satisfy equation (30) enforced by consistency condition. The loading is brought to point 'III' followed by unloading. During unloading, the damage stress $\hat{\chi}_d$ starts to retreat and yielding stops with $\hat{\kappa}$ staying at its previously experienced maximum. Since the material is already damaged, the unloading compliance is much higher than that of the intact material. One can see that the end of unloading (Figure 3, point 'IV') coincides with the starting point of this loading sequence, indicating completely recovery of the strain. It is also observed that the damage distribution at point 'IV' is identical to that at point 'III' since no further evolution occurred during unloading (Figure 4-IV). Such behavior is quite intuitive for a microcracked

solid without inelastic dissipation mechanisms such as plastic deformation in the matrix and friction along cracks.

It is worth to note that the model predicts localized microcrack accumulation along planes inclined to 45° with respect to the loading direction (Figure 4-III). The 45° direction is therefore predicted to have the highest possibility for crack coalescence and subsequent formation of a single connected fracture surface to cause the global failure and the post-failure softening of the REV (Wong 1982; Fredrich et al. 1989). Caution must be used, however, when applying the present model to describe softening behaviors. It is well known that objectively capturing the softening branch of stress-strain relation is challenging owing to the ill-posedness of the mathematical problem which leads to localized bands and mesh-dependent predictions from numerical solutions (Sulem and Vardoulakis 1995). Remediation of such ill-posedness is typically achieved by incorporating an intrinsic length scale (Bazant and Pijaudier-Cabot 1988; Pijaudier-Cabot and Benallal 1993) or time scale (Perzyna 1966; Das et al. 2013) in the constitutive laws. One way to model the strong displacement discontinuity in brittle solids is the traction based approach (Oliver et al. 2012; Wu and Cervera 2016) with volume-averaging the localized deformation over the REV (Haghighat and Pietruszczak 2015; Moallemi and Pietruszczak 2017; Zhao et al. 2018). For the present model where the onset of softening is controlled by a continuous damage distribution function, achieving objective post-peak predictions may require novel treatments on the damage evolution law such that the maximum damage does not blow up passing the peak, in addition to the usual regularization techniques or the volume-averaging treatments. Tackling these issues cannot be rushed because of the mathematical rigorousness and thermodynamic consistency required. We shall therefore focus the remainder of this first study on the hardening branch of the mechanical response to pave the way for a follow-up study on softening.

Incorporation of crack friction

As observed in section 'Continuous hyperplasticity', the frictionless model predicts maximum damage developed along planes inclined at 45°, the planes of maximum shear stress, which does not agree with most experimental results. This can be immediately improved by considering friction on the crack surfaces. To do so, the Gibbs free energy and the dissipation rate functionals must be properly modified to include frictional resistance as an internal state function. Similar to the frictionless model, we develop the free energy potential and frictional dissipation for REV with a single crack first and then upscale to the multi-crack scenario. The evolution laws for damage and frictional resistance are finally incorporated by introducing damage and frictional dissipations.

Single microcrack

Consider a REV with a single microcrack of size $2a$ and orientation ω with respect to the global coordinate system. $\sigma\prime_{ij}$ denotes its stress state with reference to $\mathbb{E}\prime$ basis defined in the same way as in Figure 1. The crack is closed and the normal stress operating at the crack surface is same as the far field stress $\sigma\prime_{22}$ as shown in Figure 5. Under such stress state, a *mobilized shear resistance*, denoted by $\hat{\tau}\prime_f$, is developed to resist the tendency of relative motion on the crack surfaces. Neglecting any cohesion, the maximum $\hat{\tau}\prime_f$ that can be mobilized in either direction is given by $\pm\mu_f\langle\sigma\prime_{22}\rangle$ with μ_f being the friction coefficient of the crack surface. Here $\langle\,\rangle$ is the Macaulay bracket such that $\langle x\rangle = x$ for $x \geq 0$ and $\langle x\rangle = 0$ for $x < 0$. The slippage (relative motion) along the crack surfaces will occur only after $\hat{\tau}\prime_f$ is fully mobilized to its limit. The shear strain contribution (in $\mathbb{E}\prime$) due to this crack slippage is denoted by $\hat{\gamma}\prime^1_f$. The rate of energy dissipated through the slippage of the crack can be expressed as

$$\hat{\phi}_f = \mu_f\langle\sigma\prime_{22}\rangle|\dot{\hat{\gamma}}\prime^1_f| = \hat{\tau}\prime_f\dot{\hat{\gamma}}\prime^1_f, \tag{37}$$

where $\hat{\tau}\prime_f = \partial\hat{\phi}_f/\partial\dot{\hat{\gamma}}\prime^1_f$ is the *dissipative mobilized shear resistance*. The yield function for frictional slippage is obtained via degenerated Legendre transformation of $\hat{\phi}_f$:

$$\hat{\bar{y}}_f\left(\hat{\bar{\tau}}\prime_f, \sigma_{ij}, \omega\right) = \hat{\bar{\tau}}\prime^2_f - (\mu_f\sigma\prime_{22})^2 \leq 0 \quad \text{or} \quad \hat{y}_f\left(\hat{\tau}\prime_f, \sigma_{ij}, \omega\right) = \hat{\tau}\prime^2_f - (\mu_f\sigma\prime_{22})^2 \leq 0. \tag{38}$$

Now let us focus on the strain contribution due to crack slippage. The general stress state can be decomposed as the superposition of two stress states as shown in Figure 5, given the linear elastic property of the solid matrix. The stress state-1 inherits all the stresses of the original state except that the far-field shear stress is replaced by the mobilized shear resistance $\hat{\tau}\prime_f$. In this state, the far-field shear stress is always equal to the shear resistance, causing no relative sliding at the crack surface. The stress state-2 is characterized by a far-field shear stress $(\tau\prime - \hat{\tau}\prime_f)$ with a shear-resistance-free (i.e. frictionless) crack surface. It can be seen that crack slippage can only occur in state-2, driven by how much the shear stress exceeds the mobilized shear resistance $\hat{\tau}\prime_f$. Specifically, consider an instance where $\hat{\tau}\prime_f$ is not fully mobilized (i.e. $|\hat{\tau}\prime_f| < \mu_f\langle\sigma\prime_{22}\rangle$). If a small increment is applied to $\tau\prime$, more frictional resistance will be mobilized, causing $\hat{\tau}\prime_f$ to increase by the same amount such that the net shear $(\tau\prime - \hat{\tau}\prime_f)$ in stress state-2 remains unchanged and thus the shear strain increment due to crack slippage $\dot{\hat{\gamma}}\prime^1_f = 0$. In this case, the total strain increment of the REV will only be contributed by the stress state-1 due to the compliance of uncracked matrix. Now consider a scenario where $\hat{\tau}\prime_f$ is already fully mobilized (i.e. $|\hat{\tau}\prime_f| = \mu_f\langle\sigma\prime_{22}\rangle$). A small increment on $\tau\prime$ in this case can no longer be transferred to $\hat{\tau}\prime_f$ and thus leading to the increase of the shear stress difference $(\tau\prime - \hat{\tau}\prime_f)$ by the same amount as $\tau\prime$. In this case, the overall strain increment

of the REV will come from stress state-2 caused by the relative displacement of the crack surface with $\dot{\hat{\gamma}}\prime_f^1 > 0$.

For frictionless cracks, $\hat{\tau}\prime_f = 0$ and thus any magnitude of $\tau\prime$ will cause a crack-slippage-induced shear strain. Therefore, the only difference between frictionless and frictional cracks is that the cause of $\dot{\hat{\gamma}}\prime_f^1$ is $\tau\prime$ for the former while it becomes $(\tau\prime - \hat{\tau}\prime_f)$ for the latter. Observing this, the Gibbs free energy of the REV with a single frictional crack can be written by simply replacing $\tau\prime$ with $(\tau\prime - \hat{\tau}\prime_f)$ in equation (11):

$$g^{*1}\left(\sigma_{ij}, \hat{\tau}\prime_f, \omega, a\right) = -\frac{1}{2} C^0_{ijkl}\sigma_{ij}\sigma_{kl} - 2b\left(\tau\prime - \hat{\tau}\prime_f\right)^2 \frac{a^2}{A}. \tag{39}$$

The slippage-induced shear strain $\hat{\gamma}\prime_f^1$ (in $\mathbb{E}\prime$ basis) is the thermodynamic conjugate to $\hat{\tau}\prime_f$:

$$\hat{\gamma}\prime_f^1 = \frac{\partial g^{*1}}{\partial \hat{\tau}\prime_f} = 4b\left(\tau\prime - \hat{\tau}\prime_f\right) \frac{a^2}{A}. \tag{40}$$

The notation g^{*1} for free energy is used to distinguish it from its alternate form g^1, obtained by replacing $\hat{\tau}\prime_f$ with $\hat{\gamma}\prime_f^1$ in the argument through a Legendre transformation:

$$g^1\left(\sigma_{ij}, \hat{\gamma}\prime_f^1, \omega, a\right) = g^{*1}\left(\sigma_{ij}, \hat{\tau}\prime_f, \omega, a\right) - \hat{\gamma}\prime_f^1 \hat{\tau}\prime_f. \tag{41}$$

Using equation equation (41) with equation (39) and substituting $\hat{\tau}\prime_f$ from equation (40) gives

$$g^1\left(\sigma_{ij}, \hat{\gamma}\prime_f^1, \omega, a\right) = -\frac{1}{2} C^0_{ijkl}\sigma_{ij}\sigma_{kl} + \frac{1}{8b}\frac{A}{a^2}(\hat{\gamma}\prime_f^1)^2 - \hat{\gamma}\prime_f^1 \tau\prime. \tag{42}$$

Substituting equations (37) and (42) into equation (20) yields the stress-strain relation

$$\varepsilon_{ij} = -\frac{\partial g^1}{\partial \sigma_{ij}} = C^0_{ijkl}\sigma_{kl} + \frac{1}{2}\xi_{ij}\hat{\gamma}\prime_f^1, \tag{43}$$

and the orthogonality condition in the form of $\hat{\tau}\prime_f = \hat{\bar{\tau}}\prime_f$. The incremental form of $\hat{\gamma}\prime_f^1$ is obtained by differentiating equation (40) with respect to time:

$$\dot{\hat{\gamma}}\prime_f^1 = 4b\left(\dot{\tau}\prime - \dot{\hat{\tau}}\prime_f\right) \frac{a^2}{A}. \tag{44}$$

On the other hand, using equation (38), the flow rule is obtained as

$$\dot{\hat{\gamma}}\prime_f^1 = \hat{\lambda}_f \frac{\partial \hat{\bar{y}}_f}{\partial \hat{\bar{\tau}}\prime_f} = 2\hat{\lambda}_f \hat{\bar{\tau}}\prime_f = 2\hat{\lambda}_f \hat{\tau}\prime_f, \tag{45}$$

where $\hat{\lambda}_f$ is the plastic multiplier for frictional slippage. When $\hat{\tau\prime}_f$ is within the frictional yield surface, we have $\dot{\hat{\gamma}}\prime_f^1 = \hat{\lambda}_f = 0$ which in combination with equation (44) gives $\dot{\hat{\tau}}\prime_f = \dot{\tau}\prime$. At frictional yielding, the rate from of $\hat{y}_f$ in equation (38) gives the consistency condition

$$\hat{\tau}\prime_f \dot{\hat{\tau}}\prime_f - \mu_f^2 \sigma\prime_{22} \dot{\sigma}\prime_{22} = 0. \tag{46}$$

Rearranging equation (46) provides the expression of $\dot{\hat{\tau}}\prime_f$:

$$\dot{\hat{\tau}}\prime_f = \begin{cases} \dot{\tau}\prime & \text{for } \hat{y}_f < 0, \\ \mu_f^2 \sigma\prime_{22} \dot{\sigma}\prime_{22} / \hat{\tau}\prime_f & \text{for } \hat{y}_f = 0 \text{ and } \dot{\hat{y}}_f = 0. \end{cases} \tag{47}$$

Substituting equation (47) in equation (44) and comparing with equation (45) gives the expression of $\hat{\lambda}_f$ for stress-controlled testing as

$$\hat{\lambda}_f = \begin{cases} 0 & \text{for } \hat{y}_f < 0, \\ 2b(a^2/A)(\dot{\tau}\prime \hat{\tau}\prime_f - \mu_f^2 \sigma\prime_{22} \dot{\sigma}\prime_{22}) / \hat{\tau}\prime_f^2 & \text{for } \hat{y}_f = 0 \text{ and } \dot{\hat{y}}_f = 0. \end{cases} \tag{48}$$

Let us examine the model response under simple shear loading path. The REV contains a horizontal crack ($\omega = 0$) and is subjected to an isotropic stress state $\sigma\prime_{11} = \sigma\prime_{22} = \sigma\prime_0$. Shear stress is applied by gradually changing $\tau\prime$. Since $\omega = 0$, $\mathbb{E}\prime = \mathbb{E}$, equation (43) reduces to $\varepsilon_{12} = C^0_{1212}\tau\prime + 0.5\hat{\gamma}\prime_f^1$. The stress-strain response ($\tau\prime$ vs ε_{12}) is sketched in Figure 6, together with the locations of $\tau\prime$ and $\hat{\tau}\prime_f$ relative to the yield surface for a few key points. Initially at point 'O', $\tau\prime$, $\hat{\tau}\prime_f$, and $\hat{\gamma}\prime_f^1$ are all zero. The first loading cycle starts at 'O' and ends at 'II'. The friction is able to resist the applied shear stress ($\dot{\tau}\prime = \dot{\hat{\tau}}\prime_f$, $\dot{\hat{\gamma}}\prime_f^1 = 0$) till 'I' so that the REV deforms with the stiffness of the uncracked solid. After point 'I', $\hat{\tau}\prime_f$ reaches its maximum value $\mu_f \sigma\prime_0$. Thus the crack slips in the forward direction ($\dot{\hat{\gamma}}\prime_f^1 > 0$) and the REV deforms with the reduced apparent stiffness for cracked solid along 'I-II'. Unloading occurs along the path 'II-III-IV'. During 'II-III', $\hat{\tau}\prime_f$ decreases with decreasing $\tau\prime$ to prevent slippage ($\dot{\tau}\prime = \dot{\hat{\tau}}\prime_f$) so that $\hat{\tau}\prime_f$ remains within the yield surface and the REV recovers to the uncracked stiffness ($\dot{\hat{\gamma}}\prime_f^1 = 0$). At point 'III', $\hat{\tau}\prime_f$ reaches the threshold value in the reverse direction ($-\mu_f \sigma\prime_0$) causing slippage in reverse direction ($\dot{\hat{\gamma}}\prime_f^1 < 0$), thus triggering the reduced apparent stiffness again. The same process repeats during reloading along 'IV-V' and 'V-VI'. All state variable have identical values at points 'II' and 'VI'.

It may appear that the frictional crack model predicts a so-called hardening stress-strain response (Figure 6) with a non-hardening yield surface (equation (38)), which seems counter-intuitive. This can be explained by highlighting the fact that the yield surface is not imposed on the shear stress $\tau\prime$, but on the mobilized shear resistance $\hat{\tau}\prime_f$ which is an internal state variable of the material. $\hat{\tau}\prime_f$ always obeys the

yield condition (equation (38)) and the flow rule dictated by the hyperplasticity principles. The resolved shear stress $\tau\prime$ which is controlled by the far-field stress, however, can change freely below $\hat{\tau}\prime_f$ for non-slipping case or exceed $\hat{\tau}\prime_f$ to cause slippage along the crack. The unbalanced shear stress $(\tau\prime - \hat{\tau}\prime_f)$ in the latter scenario is actually transferred to the stress field near the crack tip in driving the mode-II fracturing. It will be soon revealed that this term is indeed the driving force for damage growth in the next section.

Multiple microcracks

This section completes the model formulation by generalizing to multiple cracks and introduce damage evolution. The Gibbs free energy for REV with multiple frictional microcracks is obtained by applying the same upscaling procedure described in section 'Compliance of microcracked solid' on 'g^{*1}' defined in equation (39):

$$g^*[\sigma_{ij}, \hat{d}, \hat{\tau}\prime_f] = g_1(\sigma_{ij}) + \int_0^\pi \hat{g}_2^*(\sigma_{ij}, \hat{\tau}\prime_f, \hat{d}, \omega)\, d\omega, \tag{49}$$

where g_1 is still given by equation (22) and $\hat{g}_2^*$ includes the contribution of $\hat{\tau}\prime_f$:

$$\hat{g}_2^*(\sigma_{ij}, \hat{\gamma}\prime_f, \hat{d}, \omega) = -2b\,(\tau\prime - \hat{\tau}\prime_f)^2\,\hat{d}. \tag{50}$$

Similar to equation (40), the *directional sliding-induced shear strain* $\hat{\gamma}\prime_f$ is obtained by differentiating $\hat{g}_2^*$ with respect to $\hat{\tau}\prime_f$:

$$\hat{\gamma}\prime_f = \frac{\partial \hat{g}_2^*}{\partial \hat{\tau}\prime_f} = 4b\,(\tau\prime - \hat{\tau}\prime_f)\,\hat{d}. \tag{51}$$

The transformed Gibbs free energy in terms of $\hat{\gamma}\prime_f$ can be written as

$$g[\sigma_{ij}, \hat{d}, \hat{\gamma}\prime_f] = g_1(\sigma_{ij}) + \int_0^\pi \hat{g}_2(\sigma_{ij}, \hat{\gamma}\prime_f, \hat{d}, \omega)\, d\omega, \tag{52}$$

$$\text{where} \quad \hat{g}_2(\sigma_{ij}, \hat{\gamma}\prime_f, \hat{d}, \omega) = \frac{1}{8b}\frac{\hat{\gamma}\prime_f^2}{\hat{d}} - \tau\prime\hat{\gamma}\prime_f. \tag{53}$$

The incremental from of g is

$$\dot{g} = \left(\frac{\partial g_1}{\partial \sigma_{ij}} + \int_0^\pi \frac{\partial \hat{g}_2}{\partial \sigma_{ij}}\, d\omega\right)\dot{\sigma}_{ij} - \int_0^\pi \hat{\chi}_d \dot{\hat{d}}\, d\omega - \int_0^\pi \hat{\tau}\prime_f \dot{\hat{\gamma}}\prime_f\, d\omega, \tag{54}$$

where $\hat{\chi}_d = -\partial \hat{g}_2/\partial \hat{d}$ and $\hat{\tau}\prime_f = -\partial \hat{g}_2/\partial \hat{\gamma}\prime_f$ denotes the directional damage stress and the mobilized shear resistance respectively. The stored energy can be dissipated through damage growth and frictional

slippage along the microcracks. Here we propose a simple additive decomposition of the directional dissipation rate

$$\hat{\phi}(\omega, \sigma_{ij}, \dot{\hat{\gamma}}\prime_f, \dot{\hat{d}}, \hat{\kappa}) = \hat{\phi}_d(\hat{\kappa}, \dot{\hat{d}}) + \hat{\phi}_f(\omega, \sigma_{ij}, \dot{\hat{\gamma}}\prime_f), \text{ where} \tag{55}$$

$$\hat{\phi}_f(\omega, \sigma_{ij}, \dot{\hat{\gamma}}\prime_f) = \mu_f \langle \sigma\prime_{22} \rangle |\dot{\hat{\gamma}}\prime_f|, \quad \hat{\phi}_d(\hat{\kappa}, \dot{\hat{d}}) = \hat{\kappa}|\dot{\hat{d}}|. \tag{56}$$

Equation (55) is first-order homogeneous in $\dot{\hat{d}}$ and $\dot{\hat{\gamma}}\prime_f$ and thus still describes a rate-independent processes. Applying Euler's theorem to equation (55) and integrating over all direction gives the total dissipation rate

$$\phi(\sigma_{ij}, \dot{\hat{\gamma}}\prime_f, \dot{\hat{d}}, \hat{\kappa}) = \int_0^\pi \hat{\phi}\, d\omega = \int_0^\pi \left(\hat{\bar{\chi}}_d \dot{\hat{d}} + \hat{\bar{\tau}}\prime_f \dot{\hat{\gamma}}\prime_f \right) d\omega, \tag{57}$$

where $\hat{\bar{\chi}}_d = \partial \hat{\phi}_d / \partial \dot{\hat{d}}$ and $\hat{\bar{\tau}}\prime_f = \partial \hat{\phi}_f / \partial \dot{\hat{\gamma}}\prime_f$. Substituting equations (54) and (57) into equation (20) and enforcing $\hat{\bar{\tau}}\prime_f = \hat{\tau}\prime_f$ and $\hat{\chi}_d = \hat{\bar{\chi}}_d$ gives the stress-strain relation

$$\varepsilon_{ij} = C^0_{ijkl}\sigma_{kl} + \frac{1}{2}\int_0^\pi \xi_{ij}\hat{\gamma}\prime_f \, d\omega. \tag{58}$$

The degenerated Legendre transformation of $\hat{\phi}_d$ and $\hat{\phi}_f$ provides the yield functions for damage and friction respectively. The damage yield function has the same form as that of frictionless model and equations (30) to (35) are valid as well. The only difference is that the damage stress for the frictional model is updated to

$$\hat{\bar{\chi}}_d = \hat{\chi}_d = \frac{1}{8b}\frac{\hat{\gamma}\prime_f^2}{\hat{d}^2} = 2b\left(\tau\prime - \hat{\tau}\prime_f\right)^2, \tag{59}$$

according to equation (54). We can see that now it is the unbalanced shear stress $(\tau\prime - \hat{\tau}\prime_f)$ determining the damage stress rather than $\tau\prime$ as compared to the frictionless case in equation (24). It makes physical sense for reasons discussed in section 'Incorporation of crack friction'. The friction yield function has the same form as equation (38). Both $\hat{y}_d$ and $\hat{y}_f$ are now functions of orientation and therefore they must be checked for all directions. In response to arbitrary external loading, crack along some orientations will slip while cracks long other directions will not. Therefore, similar to Θ^d, the set of orientations undergoing frictional slippage is defined as

$$\Theta^f = \{\omega \in [0, \pi] \quad | \quad \hat{y}_f = 0 \text{ and } \dot{\hat{y}}_f = 0\}. \tag{60}$$

The consistency condition associated with the frictional yielding is still given by equation (46) while the flow rule of $\hat{\gamma\prime}_f$ is expressed as

$$\dot{\hat{\gamma}}\prime_f = \hat{\lambda}_f \frac{\partial \hat{\bar{y}}_f}{\partial \hat{\bar{\tau}}\prime_f} = \begin{cases} 2\hat{\lambda}_f \hat{\bar{\tau}}\prime_f = 2\hat{\lambda}_f \hat{\tau}\prime_f & \text{for}\, \omega \in \Theta^f, \\ 0 & \text{otherwise.} \end{cases} \tag{61}$$

The incremental stress-strain response is obtained from equation (58) as

$$\dot{\varepsilon}_{ij} = C^0_{ijkl}\dot{\sigma}_{kl} + \frac{1}{2}\int_0^\pi \xi_{ij}\dot{\hat{\gamma}}\prime_f \, d\omega, \text{ where} \tag{62}$$

$$\dot{\hat{\gamma}}\prime_f = 4b\left(\dot{\tau}\prime - \dot{\hat{\tau}}\prime_f\right)\hat{d} + 4b\left(\tau\prime - \hat{\tau}\prime_f\right)\dot{\hat{d}}. \tag{63}$$

The values of $\dot{\hat{\gamma}}\prime_f$, $\dot{\hat{d}}$ and $\dot{\hat{\tau}}\prime_f$ for any given direction will depend on whether the friction and/or damage yield conditions are satisfied along that direction. Their calculations can be discussed in the following four possible cases:

(1) For an orientation with $\omega \notin \Theta^f$ and $\omega \notin \Theta^d$, we have $\dot{\hat{\gamma}}\prime_f = \dot{\hat{d}} = \hat{\lambda}_f = \hat{\lambda}_d = 0$, thus there is no inelastic contribution from such direction. Substituting $\dot{\hat{\gamma}}\prime_f = \dot{\hat{d}} = 0$ in equation (63) and imposing $\hat{d} \neq 0$ gives $\dot{\hat{\tau}}\prime_f = \dot{\tau}\prime$. Also, it follows from equation (59) that $\dot{\hat{\chi}}_d = 0$ as well.

(2) For a direction with $\omega \in \Theta^f$ and $\omega \notin \Theta^d$, the expression of $\hat{\lambda}_f$ is similar to that obtained for single crack formulation with the only difference being a^2/A replaced by $\hat{d}$:

$$\hat{\lambda}_f = 2b\frac{\hat{d}}{\hat{\tau}\prime_f^2}(\dot{\tau}\prime\hat{\tau}\prime_f - \mu_f^2\sigma\prime_{22}\dot{\sigma}\prime_{22}) \quad \text{for} \quad \omega \in \Theta^f \,\text{and}\, \omega \notin \Theta^d. \tag{64}$$

Alternatively, $\dot{\hat{\tau}}\prime_f$ can be obtained directly from equation (47). $\dot{\hat{\gamma}}\prime_f$ and $\dot{\hat{\chi}}_d$ can be computed by equations (63) and (59) respectively since $\dot{\hat{d}} = \lambda_d = 0$.

(3) For a direction with $\omega \in \Theta^f$ and $\omega \in \Theta^d$, the relation between $\dot{\hat{\tau}}\prime_f$ and $\hat{\lambda}_f$ is obtained by combining equations (35), (59) and (63):

$$\dot{\hat{\tau}}\prime_f = \dot{\tau}\prime - \frac{1}{2b}\hat{\lambda}_f\hat{\tau}\prime_f\left(\hat{d} + 2\hat{\chi}_d\left(\frac{\partial\hat{\kappa}}{\partial\hat{d}}\right)^{-1}\right)^{-1}. \tag{65}$$

Substituting equation (65) into equation (46) gives

$$\hat{\lambda}_f = 2b\frac{1}{\hat{\tau\prime}_f^2}(\dot{\tau\prime}\hat{\tau\prime}_f - \mu_f^2\sigma\prime_{22}\dot{\sigma}\prime_{22})\left(\hat{d} + 2\hat{\chi}_d\left(\frac{\partial\hat{\kappa}}{\partial\hat{d}}\right)^{-1}\right) \quad \text{for} \quad \omega \in \Theta^f \text{ and } \omega \in \Theta^d. \tag{66}$$

$\dot{\hat{\tau}}\prime_f$ is obtained by substituting $\hat{\lambda}_f$ from equation (66) into equation (65) or directly from equation (47). $\dot{\hat{\chi}}_d$ is obtained from equation (59) after which $\hat{\lambda}_d$ and $\dot{\hat{d}}$ can be obtained from equations (34) and (35), respectively. Finally, $\dot{\hat{\gamma}}\prime_f$ is obtained from equation (63).

(4) For a case with only damage evolution without frictional slippage ($\omega \notin \Theta^f$, $\omega \in \Theta^d$), we have $\dot{\hat{d}} > 0$ since healing effects are not modeled in the present work. Also, $\partial\hat{\kappa}/\partial\hat{d}$ is always chosen to be strictly positive. Therefore, equation (35) implies that $\dot{\hat{\chi}}_d > 0$ which combined with the rate form of equation (59) implies that $(\tau\prime - \hat{\tau}\prime_f)(\dot{\tau}\prime - \dot{\hat{\tau}}\prime_f) > 0$ as well. Supplying $(\tau\prime - \hat{\tau}\prime_f)(\dot{\tau}\prime - \dot{\hat{\tau}}\prime_f) > 0$ and $\dot{\hat{d}} > 0$ in equation (63) gives $\dot{\hat{\gamma}}\prime_f \neq 0$. This contradicts with the initial assumption that frictional yielding is not triggered. This makes physical sense as microcracks cannot grow without relative displacement along the crack surface. Therefore, the forth case with $\omega \notin \Theta^f$ and $\omega \in \Theta^d$ will never occur. In other words, we have proven that $\Theta^d \subseteq \Theta^f \subseteq [0, \pi]$ and the three cases discussed above are exhaustive. Physically, this implies that the dissipation through damage evolution is always accompanied by frictional dissipation which in agreement with experimental observations (Landis et al. 2019).

Finally, to account for the pressure dependence of crack propagation in compressive loading, the following hardening function $\partial\kappa/\partial\hat{d}$ is proposed:

$$\frac{\partial\hat{\kappa}}{\partial\hat{d}} = \kappa_m\left(\frac{r}{\sigma_m}\right)^e \exp\left[-\hat{d}\left(\frac{r}{\sigma_m}\right)^e\right], \tag{67}$$

where $\sigma_m = (\sigma_{11} + \sigma_{22})/2$ is the mean stress; κ_m represents the difference of the value of κ at failure to its value for an undamaged material; r and e control the effect of mean stress on the hardening function and thus adjust the sharpness of the stress-strain response near failure.

Application of the directional damage model

Biaxial compression of Gosford sandstone

The proposed directional friction-damage model is used to simulate the biaxial compression behavior of Gosford sandstone obtained Ord et al. (1991). Their biaxial compression test consists of an initial isotropic compression phase in which σ_{11} and σ_{22} are increased together to reach the confining pressure $\sigma_0 = 10MPa$. Then σ_{11} is kept constant at σ_0 and two loading-unloading-reloading cycles are applied on σ_{22}. The experimental data and the simulation results are plotted in Figure 7. The initial damage

distribution $\hat{d}(\omega) = d_0$, $\forall\omega \in [0, \pi]$ and the initial damage threshold $\hat{\kappa}(\omega) = \kappa_0$, $\forall\omega \in [0, \pi]$ are chosen to represent an initially isotropic material. The elastic constants of the intact matrix (μ, ν) are calibrated based on the linear part of the unloading curve. The friction coefficient μ_f is obtained by looking at the stress at the initiation of frictional slippage (point 'I' in Figure 7). At point 'I', microcracks along some orientations will start to slip, causing increased compliance in the stress-strain curve. This increase in compliance is proportional to the number of mobilized microcracks and thus proportional to d_0. Therefore d_0 is calibrated through this increase of compliance in the stress-strain curve at point 'I' in Figure 7. The stress at the onset of damage (i.e. the beginning of strong nonlinearity, just below point 'II' in Figure 7) is proportional to κ_0 and thus is used to calibrate κ_0. The damage evolution parameters κ_m, r, and e can be obtained from the stress and strain values at the peak if biaxial compression results for different confining stresses are available. Here, these parameters are determined by best matching the peak stress, peak strain and the width of the hysteresis curve. The width of the hysteresis loop is proportional to the extent of microcracking and therefore serves as an indicator of the accumulated damage. The model parameters used to capture the Gosford sandstone data are listed in Table 2.

The directional distribution of $\tau\prime$, $\hat{\tau}\prime_f$, $\mu_f\langle\sigma\prime_{22}\rangle$, $\hat{\chi}_d$, $\hat{\kappa}$, $\hat{d}$, and $\hat{\gamma}\prime_f$ at several characteristic points are plotted in Figure 8. Figure 8-I shows these functions at point I. It is observed that the frictional shear stress is fully mobilized ($\hat{\tau}\prime_f = \mu_f\sigma\prime_{22}$) along some orientations. Therefore, Point 'I' in Figure 7 marks the onset of frictional slippage. Before point 'I', the material deforms with the uncracked material stiffness. From point 'I' to 'II', the frictional yielding continues with increasing $(\tau\prime - \hat{\tau}\prime_f)$, thus growing $\hat{\gamma}\prime_f$ and $\hat{\chi}_d$ along $\omega \in \Theta^f$. At point 'II', $\hat{\chi}_d$ has reached the yield value for some directions, resulting in a small increase in $\hat{d}$ along $\omega \in \Theta^d$ as shown in Figure 8-'II'. During the unloading branch started at point 'II', both $\tau\prime$ and $\mu_f\langle\sigma\prime_{22}\rangle$ initially shrink but $\tau\prime$ decreases faster $\forall\omega$, resulting in unloading on the frictional yield surface ($\hat{y}_d < 0\,\forall\omega$), thus the material unloads with uncracked material stiffness and $\dot{\tau}\prime = \dot{\hat{\tau}}\prime_f$. Since $\tau\prime \geq \hat{\tau}\prime_f\,\forall\omega$ at point 'II' and $\dot{\tau}\prime = \dot{\hat{\tau}}\prime_f$ during the friction unloading right after point 'II', for some orientations $\hat{\tau}\prime_f$ becomes zero and fully mobilizes in the reverse direction while $\tau\prime > 0$ (Figure 8-III). Thus, nonlinearity starts to appear in the unloading branch with $\dot{\hat{\gamma}}\prime_f < 0$ for $\omega \in \Theta^f$. The set Θ^f enlarges with continued unloading (Figure 8-IV), increasing the nonlinearity till the end of unloading at point 'IV'. Upon reloading, $\hat{\tau}\prime_f$ increases in forward direction but remains within the yield surface ($\hat{y}_f < 0\,\forall\omega$) till point 'V' and the material deforms with uncracked stiffness again. At point 'V' $\hat{\tau}\prime_f$ is fully mobilized along some orientations and nonlinearity appears with $\dot{\hat{\gamma}}\prime_f > 0$ for $\omega \in \Theta^f$ as shown in Figure 8-V. The reloading curve eventually unites with the loading curve at point 'VI' with all the state functions being identical to point 'II' as shown in Figure 8-II,VI. $\hat{d}$ did not evolve during the unloading reloading loop from point 'II' to 'VI' because $\hat{\chi}_d$ remained within the yield surface along all orientation. Damage evolution resumes at point 'VI' as shown in Figure 8-VI.

The distributions of internal states at the peak point 'VII' are plotted in Figure 8-'VII'. The maxima of $\hat{d}$ and $\hat{\gamma}'_f$ occurs along planes inclined at angles of $\omega_f = \pm 55.5^\circ$ with respect to the horizontal plane. If one considers the maxima of damage as the precursor to the formation of localized discontinuity, this result coincides with the failure plane orientation predicted by the Mohr-Coulomb (MC) criterion for triaxial conditions $\omega_f = \pm\left(\pi/4 + (tan^{-1}\mu_f)/2\right)$ with $\tan^{-1}(\mu_f)$ being the corresponding angle of internal friction. This intriguing result can be explained by considering the friction on the microcrack surface. For an initially isotropic material ($\hat{d} = d_0$, $\hat{\kappa} = \kappa_0$), both $\hat{\gamma}'_f$ and $\hat{d}$ attain their maxima at ω where $(\tau' - \hat{\tau}'_f)$ is maximum. Since $\hat{\tau}'_f$ is fully mobilized on the failure plane (i.e. $\hat{\tau}'_f = \mu_f \sigma'_{22}$), it follows that the maxima of $\hat{d}$ and $\hat{\gamma}'_f$must align along the plane with $(\tau' - \mu_f \sigma'_{22})_{max}$. It is straightforward to show that this yields the same result for ω_f as if the entire REV is described by the MC criterion. One should note that the similarity between this model and the MC criterion is only on the predicted orientation of the failure plane ω_f. The stress state at failure predicted by the damage model, in general, will not lie on an MC failure line.

Biaxial compression of Red Wildmoor sandstone

In this section, the simulation results of biaxial compression tests on Red Wildmoor sandstone under confining stresses 3.5 MPa, 10 MPa, and 15 MPa are presented and compared with the experimental data from Labuz and Dai (2000). The test set up is similar to that in subsection 'Biaxial compression of Gosford sandstone'. The elastic parameters (μ, ν) are obtained from the initial linear part of the stress-strain curve. The material is again assumed to be isotropic prior to the loading and the calibration of μ_f, d_0, and κ_0 follows the same procedure as described in the previous subsection. Damage evolution parameters κ_m, r and e are calibrated by matching the stress and strain at peak for the three curves. The model parameters are listed in Table 3.

Firstly, it is observed that the onset of nonlinearity and the corresponding slope for all three curves in Figure 9 are successfully captured by a single frictional parameter μ_f and a single initial damage d_0, as highlighted by the magnified section of stress-strain curves. Similarly, the stress levels at the onset of damage evolution for all curves are well captured by a unique κ_0 value. Second, the pressure dependence exhibited in the experimental data is well captured by the model in terms of the increase of stress levels at the onset of crack slippage, damage evolution, and the peak stress and strain levels. For all confining stresses, the maximum $\hat{d}$ and $\hat{\tau}'_f$ occurs at $\omega_f = \pm\left(\pi/4 + (tan^{-1}\mu_f)/2\right) \approx \pm 53.7^0$, while the peak values of $\hat{d}$ and $\hat{\gamma}'_f$ are higher for higher confining stress as shown in Figure (10). This pressure dependency is a combined result of 1) the dependence of frictional yielding on the normal stress on crack surface (i.e. σ'_{22}) evident from the divergence of the three curves prior to the onset of damage evolution in Figure 9, and 2) the pressure dependency in the damage evolution law in equation (67). As discussed

in the previous section, the focus of this study is the pre-failure stage and the capturing of the post-peak localization will be tackled in a future work.

Complex loading path on intact rock

To demonstrate the model capability in simulating complex stress paths, we perform a test with biaxial compression followed by simple shear. Practically, rocks near a fault zone may undergo such stress history due to movements along an active fault. In this test, a stress-free sample is isotropically loaded to $\sigma_{11} = \sigma_{22} = 10MPa$, followed by increasing σ_{22} to $160MPa$ while keeping σ_{11} constant. Finally, shear stress σ_{12} is applied to failure ($\sigma_{12} = 29.55MPa$) while keeping $\sigma_{11} = 10MPa$ and $\sigma_{22} = 160MPa$ fixed. The model parameters of Gosford sandstone (Table 2) are used here except the initial isotropic damage d_0 is set to zero. This is to show that the model performs well for vanishingly small value of initial damage. Since no seed damage is assumed, initially the material deforms linear-elastically with undamaged stiffness for biaxial loading as shown in Figure 11a. The stress-strain curve becomes nonlinear at the onset of damage and becomes more nonlinear as more damage is developed till the end of biaxial loading. Due to the damage accumulated in the biaxial stage, the shear-stress-strain curve in simple shear loading shows large nonlinearity and fails quickly at relatively low shear stress as shown in Figure 11b. The distributions $\tau\prime$, $\hat{\tau}\prime_f$, $\mu_f\langle\sigma\prime_{22}\rangle$, $\hat{\chi}_d$, $\hat{\kappa}$, $\hat{d}$, and $\hat{\gamma}\prime_f$ at the end of biaxial and simple shear loading are plotted in Figure 12a and Figure 12b respectively. The distributions at the end of biaxial loading are similar to previous simulations. However, during the simple shear, the principal stress axes undergo rotation and the symmetry axis of $\tau\prime$ and $\mu_f\langle\sigma\prime_{22}\rangle$ rotate as well since the stress components along any plane (i.e. $\sigma\prime_{22}$ and $\tau\prime$) depends on the orientation and the magnitude of the principal stresses. This results in a quite irregular shape of $\hat{d}$ and $\hat{\gamma}\prime_f$ due to the directional evolution of $\hat{\tau}\prime_f$ and $\hat{\chi}_d$. The maxima of $\hat{d}$ and $\hat{\gamma}\prime_f$ is realigned along $\omega \approx 43^\circ$ and -67°. This corresponds to the prediction of localized failure along two planes closer to the vertical and horizontal plane respectively. The irregular shape of the final damage distribution in Figure 12b caused by a complex loading path cannot be represented by a second or fourth order damage tensor. In fact, a fourth order damage tensor can only predict two peaks that are perpendicular to each other in the rosette diagram (Lubarda and Krajcinovic 1993), which cannot even capture the damage distribution after simple biaxial loading as shown in Figure 8 and Figure 10. This demonstrates the unique ability of the model in describing the distribution of microcracking and damage evolution patterns subjected to complex loading paths involving multi-stage loading and principal stress rotation that are frequently experienced by geological materials.

Conclusions

A new continuum damage model based on the concept of directional damage is presented, offering new capabilities in representing the micromechanics and the anisotropic nature of material damage. The state of damage is directly represented through the continuous directional distribution density of microcracks. Change in compliance due to microcracking is obtained through statistical homogenization under the noninteracting assumption, followed by which the concept of directional damage $\hat{d}$ is defined. The effective compliance of cracked material is also equivalently expressed through the Gibbs free energy functional. Casting the model in energy form enables us to leverage the framework of continuous hyperplasticity to explore the evolution problem, with the advantage of strictly satisfying the second law of thermodynamics via a non-negative dissipation rate functional. Friction is introduced at micro-scale along the crack face by considering the energy dissipation through frictional sliding. The yield conditions and the evolution laws of damage and slide-induced shear strain are obtained from the dissipation rate combined with the orthogonality condition.

The model is able to captures the typical stress-strain response of brittle materials, such as Gosford sandstone and Red Wildmoor sandstone. With only 8 parameters, the model simultaneously reproduces the nonlinearity, the loading-unloading hysteresis, and the pressure dependence of their stress-strain responses. Furthermore, the model offers predictions on the directional statistics of microscale features such as microcrack density and frictional strains, which indicates the orientation of potential localized failure plane for incorporating strong discontinuity and softening in future generalizations. Thanks to the micromechanical basis of the theory, the parameters of the model preserve clear physical meanings. The model can be also used for predicting the intensity and the orientation of damage evolution along complex stress paths, the pattern of which usually cannot be accurately represented by forth or even higher order damage tensors.

The present basic microcrack damage model is susceptible for numerous extensions. For example, the same mathematical structure can be used for constructing the 3D version of this model. To do so, the compliance change of a 3D elastic solid due to a penny-shaped microcrack shall be used as the basic solution and later upscaled through the directional damage function that collects the normal, size and density information of microcracks over the entire solid angle 4π. Challenge expected for such generalization lies in its numerical implementation, since more directional discretization is needed. The same upscaling strategy can be also used to incorporate other micromechanical processes. For example, the mode-I crack opening and unilateral effect can be included by enriching the crack displacement function used in deriving the compliance change. Rate-dependent damage growth can be considered by leveraging higher-order homogeneous dissipation functions, as outlined by Zhang and Buscarnera (2017) and Arson (2020).

Prepared using sagej.cls

Funding

This work was supported by the U.S. Department of Energy through grant DE NE0008771.

Declaration of conflicting interests

The authors declare that they have no known competing financial interests or personal relationships that could have appeared to influence the work reported in this paper.

References

Al-Rub RKA and Voyiadjis GZ (2003) On the coupling of anisotropic damage and plasticity models for ductile materials. *International Journal of Solids and Structures* 40(11): 2611 – 2643. DOI:https://doi.org/10.1016/S0020-7683(03)00109-4.

Arson C (2020) Micro-macro mechanics of damage and healing in rocks. *Open Geomechanics* 2. DOI: 10.5802/ogeo.4.

Ashby MF and Sammis CG (1990) The damage mechanics of brittle solids in compression. *pure and applied geophysics* 133(3): 489–521. DOI:10.1007/BF00878002.

Bažant ZP and Prat PC (1988) Microplane model for brittle‐plastic material: I. theory. *Journal of Engineering Mechanics* 114(10): 1672–1688. DOI:10.1061/(ASCE)0733-9399(1988)114:10(1672).

Bazant ZP and Pijaudier-Cabot G (1988) Nonlocal Continuum Damage, Localization Instability and Convergence. *Journal of Applied Mechanics* 55(2): 287–293. DOI:10.1115/1.3173674.

Bikong C, Hoxha D and Shao J (2015) A micro-macro model for time-dependent behavior of clayey rocks due to anisotropic propagation of microcracks. *International Journal of Plasticity* 69: 73 – 88. DOI: https://doi.org/10.1016/j.ijplas.2015.02.001.

Børvik T, Hopperstad O, Berstad T and Langseth M (2001) A computational model of viscoplasticity and ductile damage for impact and penetration. *European Journal of Mechanics - A/Solids* 20(5): 685 – 712. DOI: https://doi.org/10.1016/S0997-7538(01)01157-3.

Budiansky B and O'connell RJ (1976) Elastic moduli of a cracked solid. *International Journal of Solids and Structures* 12(2): 81 – 97. DOI:https://doi.org/10.1016/0020-7683(76)90044-5.

Bui T, Wong H, Deleruyelle F, Xie L and Tran D (2017) A thermodynamically consistent model accounting for viscoplastic creep and anisotropic damage in unsaturated rocks. *International Journal of Solids and Structures* 117: 26 – 38. DOI:https://doi.org/10.1016/j.ijsolstr.2017.04.015.

Carol I, Prat PC and López CM (1997) Normal/shear cracking model: Application to discrete crack analysis. *Journal of Engineering Mechanics* 123(8): 765–773. DOI:10.1061/(ASCE)0733-9399(1997)123:8(765).

Prepared using sagej.cls

Castañeda P and Willis J (1995) The effect of spatial distribution on the effective behavior of composite materials and cracked media. *Journal of the Mechanics and Physics of Solids* 43(12): 1919 – 1951. DOI:https://doi.org/10.1016/0022-5096(95)00058-Q.

Chau KT and Wong RHC (1997) Effective moduli of microcracked rocks: Theories and experiments. *International Journal of Damage Mechanics* 6(3): 258–277. DOI:10.1177/105678959700600303.

Cicekli U, Voyiadjis GZ and Al-Rub RKA (2007) A plasticity and anisotropic damage model for plain concrete. *International Journal of Plasticity* 23(10): 1874 – 1900. DOI:https://doi.org/10.1016/j.ijplas.2007.03.006.

Collins IF and Houlsby GT (1997) Application of thermomechanical principles to the modelling of geotechnical materials. *Proceedings of the Royal Society of London. Series A: Mathematical, Physical and Engineering Sciences* 453(1964): 1975–2001. DOI:10.1098/rspa.1997.0107.

Das A, Nguyen GD and Einav I (2013) The propagation of compaction bands in porous rocks based on breakage mechanics. *Journal of Geophysical Research: Solid Earth* 118(5): 2049–2066. DOI:10.1002/jgrb.50193.

David E, Brantut N, Schubnel A and Zimmerman R (2012) Sliding crack model for nonlinearity and hysteresis in the uniaxial stress–strain curve of rock. *International Journal of Rock Mechanics and Mining Sciences* 52: 9 – 17. DOI:https://doi.org/10.1016/j.ijrmms.2012.02.001.

Einav I, Houlsby G and Nguyen G (2007) Coupled damage and plasticity models derived from energy and dissipation potentials. *International Journal of Solids and Structures* 44(7): 2487 – 2508. DOI:https://doi.org/10.1016/j.ijsolstr.2006.07.019.

Einav I and Puzrin A (2004) Continuous hyperplastic critical state (chcs) model: Derivation. *International Journal of Solids and Structures* 41(1): 199 – 226. DOI:https://doi.org/10.1016/j.ijsolstr.2003.09.012.

Fanella D and Krajcinovic D (1988) A micromechanical model for concrete in compression. *Engineering Fracture Mechanics* 29(1): 49 – 66. DOI:https://doi.org/10.1016/0013-7944(88)90006-9.

Fredrich JT, Evans B and Wong TF (1989) Micromechanics of the brittle to plastic transition in carrara marble. *Journal of Geophysical Research: Solid Earth* 94(B4): 4129–4145. DOI:10.1029/JB094iB04p04129.

Haghighat E and Pietruszczak S (2015) On modeling of discrete propagation of localized damage in cohesive-frictional materials. *International Journal for Numerical and Analytical Methods in Geomechanics* 39(16): 1774–1790. DOI:10.1002/nag.2368.

Horii H and Nemat-Nasser S (1983) Overall moduli of solids with microcracks: Load-induced anisotropy. *Journal of the Mechanics and Physics of Solids* 31(2): 155 – 171. DOI:https://doi.org/10.1016/0022-5096(83)90048-0.

Horii H, Nemat-Nasser S and Ashby MF (1986) Brittle failure in compression: splitting faulting and brittle-ductile transition. *Philosophical Transactions of the Royal Society of London. Series A, Mathematical and Physical Sciences* 319(1549): 337–374. DOI:10.1098/rsta.1986.0101.

Houlsby G and Puzrin A (2007) *Principles of hyperplasticity: An approach to plasticity theory based on thermodynamic principles*. Springer London. DOI:https://doi.org/10.1007/978-1-84628-240-9.

Houlsby GT (2014) *Beyond the Second Law: Entropy Production and Non-equilibrium Systems*, chapter Dissipation Rate Functions, Pseudopotentials, Potentials and Yield Surfaces. Springer Berlin Heidelberg. ISBN 978-3-642-40154-1, pp. 73–95. URL https://doi.org/10.1007/978-3-642-40154-1_4.

Hoxha D, Lespinasse M, Sausse J and Homand F (2005) A microstructural study of natural and experimentally induced cracks in a granodiorite. *Tectonophysics* 395(1): 99 – 112. DOI:https://doi.org/10.1016/j.tecto.2004.09.004.

Jin W and Arson C (2017) Discrete equivalent wing crack based damage model for brittle solids. *International Journal of Solids and Structures* 110-111: 279 – 293. DOI:https://doi.org/10.1016/j.ijsolstr.2016.12.025.

Jin W and Arson C (2018) Micromechanics based discrete damage model with multiple non-smooth yield surfaces: Theoretical formulation, numerical implementation and engineering applications. *International Journal of Damage Mechanics* 27(5): 611–639. DOI:10.1177/1056789517695872.

Ju J (1989) On energy-based coupled elastoplastic damage theories: Constitutive modeling and computational aspects. *International Journal of Solids and Structures* 25(7): 803 – 833. DOI:https://doi.org/10.1016/0020-7683(89)90015-2.

Ju J (1991) On two-dimensinal self-consistent micromechanical damage models for brittle solids. *International Journal of Solids and Structures* 27(2): 227 – 258. DOI:https://doi.org/10.1016/0020-7683(91)90230-D.

Kachanov M (1993) *Elastic Solids with Many Cracks and Related Problems*, *Advances in Applied Mechanics*, volume 30. Elsevier. DOI:https://doi.org/10.1016/S0065-2156(08)70176-5.

Kachanov ML (1958) On the creep rupture time. *Izv Akad, Nauk USSR Otd, Tech 8* : 26–31.

Kachanov ML (1982) A microcrack model of rock inelasticity part i: Frictional sliding on microcracks. *Mechanics of Materials* 1(1): 19 – 27. DOI:https://doi.org/10.1016/0167-6636(82)90021-7.

Krajcinovic D (1996) *Damage Mechanics*. North-Holland Series in Applied Mathematics and Mechanics. North-Holland.

Labuz JF and Dai ST (2000) Residual strength and fracture energy from plane-strain testing. *Journal of Geotechnical and Geoenvironmental Engineering* 126(10): 882–889. DOI:10.1061/(ASCE)1090-0241(2000)126:10(882).

Landis EN, Kravchuk R and Loshkov D (2019) Experimental investigations of internal energy dissipation during fracture of fiber-reinforced ultra-high-performance concrete. *Frontiers of Structural and Civil Engineering* 13: 190 – 200. DOI:10.1007/s11709-018-0487-1.

Lemaitre J (2012) *A Course on Damage Mechanics*. 2 edition. Springer-Verlag Berlin Heidelberg.

Lubarda V and Krajcinovic D (1993) Damage tensors and the crack density distribution. *International Journal of Solids and Structures* 30(20): 2859 – 2877. DOI:https://doi.org/10.1016/0020-7683(93)90158-4.

Moallemi S and Pietruszczak S (2017) Analysis of localized fracture in 3d reinforced concrete structures using volume averaging technique. *Finite Elements in Analysis and Design* 125: 41 – 52. DOI:https://doi.org/10.1016/j.finel.2016.10.004.

Nguyen GD and Houlsby GT (2008) A coupled damage–plasticity model for concrete based on thermodynamic principles: Part i: model formulation and parameter identification. *International Journal for Numerical and Analytical Methods in Geomechanics* 32(4): 353–389. DOI:10.1002/nag.627.

Ožbolt J and Bažant ZP (1992) Microplane model for cyclic triaxial behavior of concrete. *Journal of Engineering Mechanics* 118(7): 1365–1386. DOI:10.1061/(ASCE)0733-9399(1992)118:7(1365).

Oliver J, Huespe A and Dias I (2012) Strain localization, strong discontinuities and material fracture: Matches and mismatches. *Computer Methods in Applied Mechanics and Engineering* 241-244: 323 – 336. DOI: https://doi.org/10.1016/j.cma.2012.06.004.

Ord A, Vardoulakis I and Kajewski R (1991) Shear band formation in gosford sandstone. *International Journal of Rock Mechanics and Mining Sciences and Geomechanics Abstracts* 28(5): 397 – 409. DOI:https://doi.org/10.1016/0148-9062(91)90078-Z.

Paliwal B and Ramesh K (2008) An interacting micro-crack damage model for failure of brittle materials under compression. *Journal of the Mechanics and Physics of Solids* 56(3): 896 – 923. DOI:https://doi.org/10.1016/j.jmps.2007.06.012.

Pardoen B, Talandier J and Collin F (2016) Permeability evolution and water transfer in the excavation damaged zone of a ventilated gallery. *International Journal of Rock Mechanics and Mining Sciences* 85: 192 – 208. DOI:https://doi.org/10.1016/j.ijrmms.2016.03.007.

Pense SL, Arson C and Pouya A (2016) A fully coupled damage-plasticity model for unsaturated geomaterials accounting for the ductile–brittle transition in drying clayey soils. *International Journal of Solids and Structures* 91: 102 – 114. DOI:https://doi.org/10.1016/j.ijsolstr.2016.04.007.

Perzyna P (1966) *Fundamental Problems in Viscoplasticity*, *Advances in Applied Mechanics*, volume 9. Elsevier. DOI:https://doi.org/10.1016/S0065-2156(08)70009-7.

Pijaudier-Cabot G and Benallal A (1993) Strain localization and bifurcation in a nonlocal continuum. *International Journal of Solids and Structures* 30(13): 1761 – 1775. DOI:https://doi.org/10.1016/0020-7683(93)90232-V.

Puzrin A and Houlsby G (2001a) Fundamentals of kinematic hardening hyperplasticity. *International Journal of Solids and Structures* 38(21): 3771 – 3794. DOI:https://doi.org/10.1016/S0020-7683(00)00238-9.

Puzrin A and Houlsby G (2001b) A thermomechanical framework for rate-independent dissipative materials with internal functions. *International Journal of Plasticity* 17(8): 1147 – 1165. DOI:https://doi.org/10.1016/S0749-6419(00)00083-8.

Sammis C and Ashby M (1986) The failure of brittle porous solids under compressive stress states. *Acta Metallurgica* 34(3): 511 – 526. DOI:https://doi.org/10.1016/0001-6160(86)90087-8.

Shao J and Rudnicki J (2000) A microcrack-based continuous damage model for brittle geomaterials. *Mechanics of Materials* 32(10): 607 – 619. DOI:https://doi.org/10.1016/S0167-6636(00)00024-7.

Sulem J and Vardoulakis IG (1995) *Bifurcation analysis in geomechanics*. CRC Press.

Prepared using sagej.cls

Sumarac D and Krajcinovic D (1987) A self-consistent model for microcrack-weakened solids. *Mechanics of Materials* 6(1): 39 – 52. DOI:https://doi.org/10.1016/0167-6636(87)90021-4.

Tsang C, Barnichon J, Birkholzer J, Li X, Liu H and Sillen X (2012) Coupled thermo-hydro-mechanical processes in the near field of a high-level radioactive waste repository in clay formations. *International Journal of Rock Mechanics and Mining Sciences* 49: 31 – 44. DOI:https://doi.org/10.1016/j.ijrmms.2011.09.015.

Voyiadjis GZ, Shojaei A and Li G (2011) A thermodynamic consistent damage and healing model for self healing materials. *International Journal of Plasticity* 27(7): 1025 – 1044. DOI:https://doi.org/10.1016/j.ijplas.2010.11.002.

Voyiadjis GZ, Taqieddin ZN and Kattan PI (2008) Anisotropic damage–plasticity model for concrete. *International Journal of Plasticity* 24(10): 1946 – 1965. DOI:https://doi.org/10.1016/j.ijplas.2008.04.002.

Walsh JB (1965) The effect of cracks on the uniaxial elastic compression of rocks. *Journal of Geophysical Research (1896-1977)* 70(2): 399–411. DOI:10.1029/JZ070i002p00399.

Wong TF (1982) Micromechanics of faulting in westerly granite. *International Journal of Rock Mechanics and Mining Sciences and Geomechanics Abstracts* 19(2): 49 – 64. DOI:https://doi.org/10.1016/0148-9062(82)91631-X.

Wu JY and Cervera M (2016) A thermodynamically consistent plastic-damage framework for localized failure in quasi-brittle solids: Material model and strain localization analysis. *International Journal of Solids and Structures* 88-89: 227 – 247. DOI:https://doi.org/10.1016/j.ijsolstr.2016.03.005.

Yazdani S and Schreyer H (1988) An anisotropic damage model with dilatation for concrete. *Mechanics of Materials* 7(3): 231 – 244. DOI:https://doi.org/10.1016/0167-6636(88)90022-1.

Zhang YD and Buscarnera G (2017) A rate-dependent breakage model based on the kinetics of crack growth at the grain scale. *Géotechnique* 67(11): 953–967. DOI:10.1680/jgeot.16.P.181.

Zhao LY, Shao JF and Zhu QZ (2018) Analysis of localized cracking in quasi-brittle materials with a micro-mechanics based friction-damage approach. *Journal of the Mechanics and Physics of Solids* 119: 163 – 187. DOI:https://doi.org/10.1016/j.jmps.2018.06.017.

Zhu C and Arson C (2014) A thermo-mechanical damage model for rock stiffness during anisotropic crack opening and closure. *Acta Geotechnica* 9(5): 847–867. DOI:10.1007/s11440-013-0281-0.

Zhu C and Arson C (2015) A model of damage and healing coupling halite thermo-mechanical behavior to microstructure evolution. *Geotechnical and Geological Engineering* 33(2): 389–410. DOI:10.1007/s10706-014-9797-9.

Zhu Q and Shao J (2016) Micromechanics of rock damage: Advances in the quasi-brittle field. *Journal of Rock Mechanics and Geotechnical Engineering* 9(1): 29 – 40. DOI:https://doi.org/10.1016/j.jrmge.2016.11.003.

Zhu QZ, Kondo D and Shao JF (2009) Homogenization-based analysis of anisotropic damage in brittle materials with unilateral effect and interactions between microcracks. *International Journal for Numerical and Analytical*

Methods in Geomechanics 33(6): 749–772. DOI:10.1002/nag.741.

Tables

Table 1. Model parameters for frictionless damage model simulation.

Parameter	μ	ν	κ_0	d_0	$\partial\kappa/\partial\hat{d}$
	GPa		kPa		kPa
Value	24	0.33	50	0	500

Table 2. Model parameters for Gosford sandstone.

Parameter	μ	ν	κ_0	d_0	μ_f	κ_m	r	e
	GPa		kPa			kPa	GPa	
Value	5.5	0.43	30	0.5	0.4	400	0.79	0.5

Table 3. Model parameters for Red Wildmoor sandstone.

Parameter	μ	ν	κ_0	d_0	μ_f	κ_m	r	e
	GPa		kPa			kPa	GPa	
Value	4.29	0.17	15	0.8	0.32	100	0.055	0.7

Figures

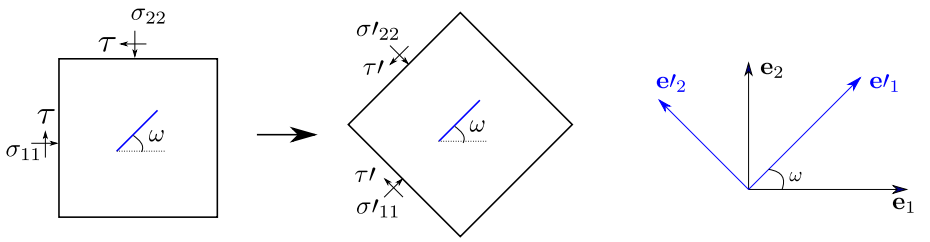

Figure 1. Stress components in local and global coordinate system.

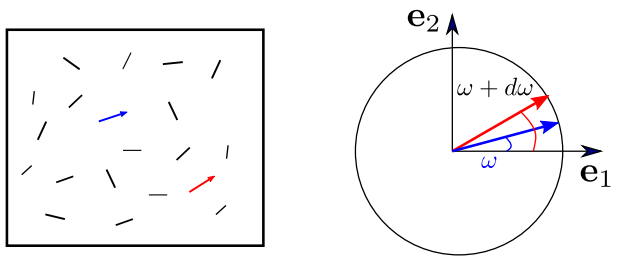

Figure 2. Schematic of microcrack distribution in the REV.

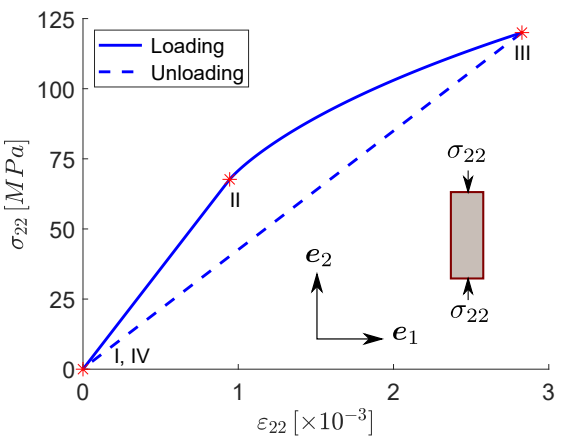

Figure 3. Axial stress-strain response in uniaxial plane strain compression from frictionless damage model.

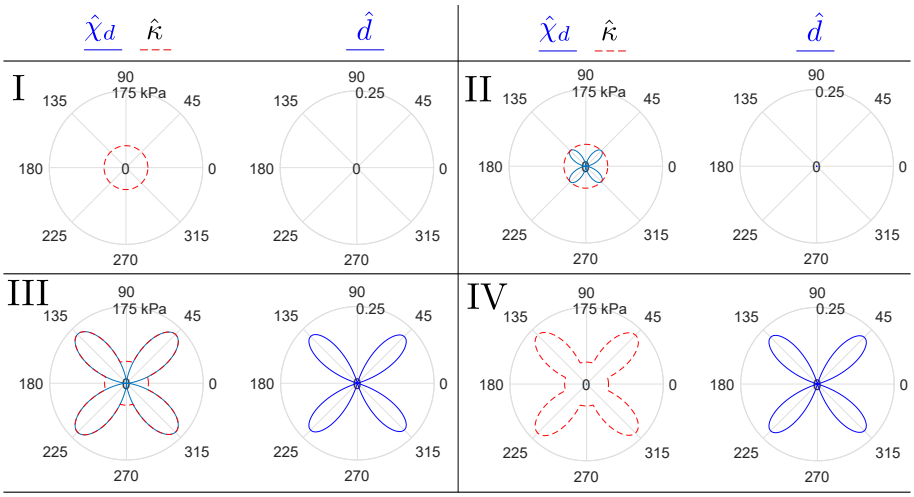

Figure 4. Plots of $\hat{\chi}_d$, $\hat{\kappa}$ and $\hat{d}$ at points 'I', 'II', 'II', and 'IV' in Figure 3.

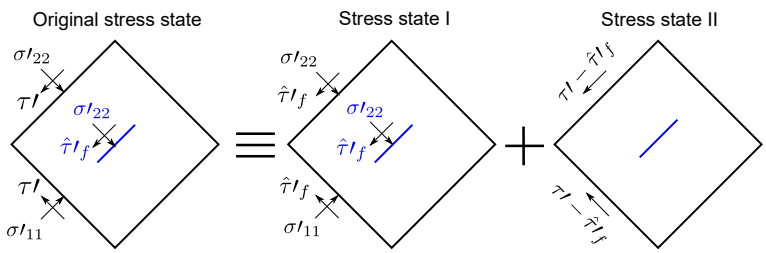

Figure 5. Simple decomposition of stress components in the local coordinate system.

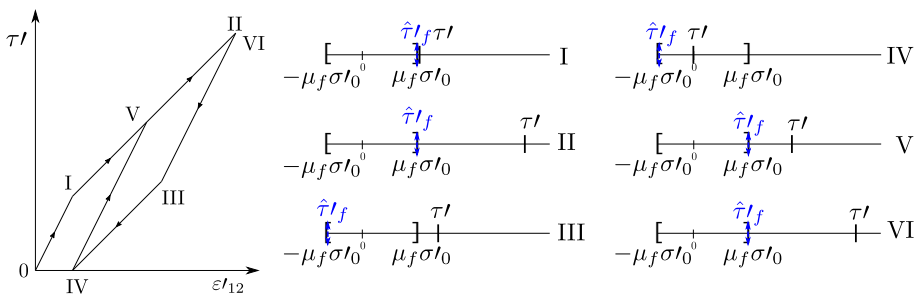

Figure 6. Schematic of single frictional microcrack model response to simple shear stress path in local coordinate system.

Prepared using sagej.cls

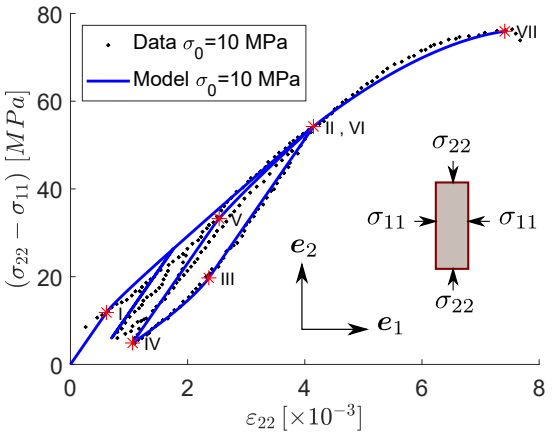

Figure 7. Simulation results for biaxial compression of Gosford sandstone.

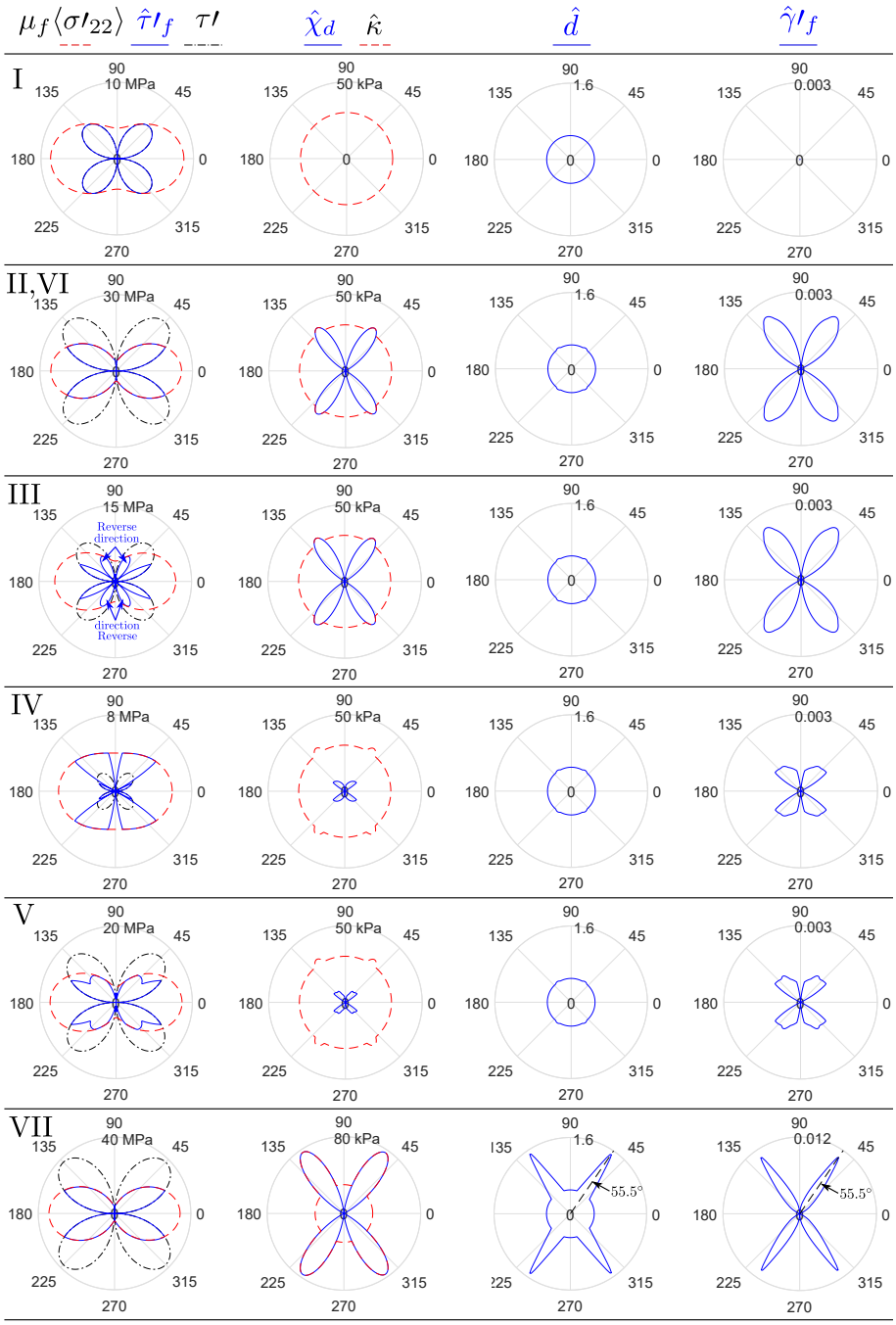

Figure 8. Plots of $\tau\prime$, $\hat{\tau}\prime_f$, $\mu_f\langle\sigma\prime_{22}\rangle$, $\hat{\chi}_d$, $\hat{\kappa}$, $\hat{d}$, and $\hat{\gamma}\prime_f$ at selected points in Figure 7.

Prepared using sagej.cls

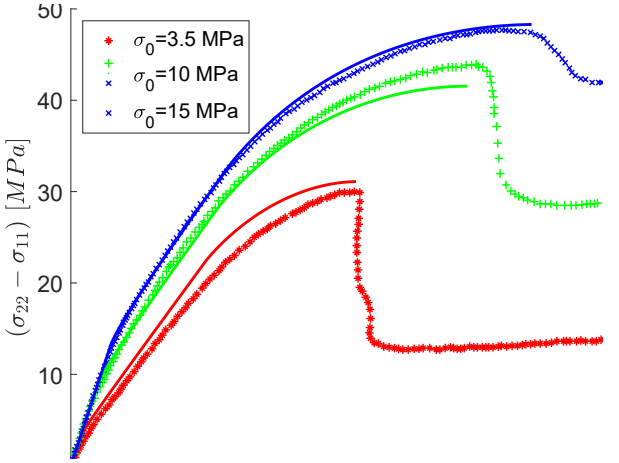

Figure 9. Simulation results for biaxial compression of Red Wildmoor sandstone under various initial confining stresses.

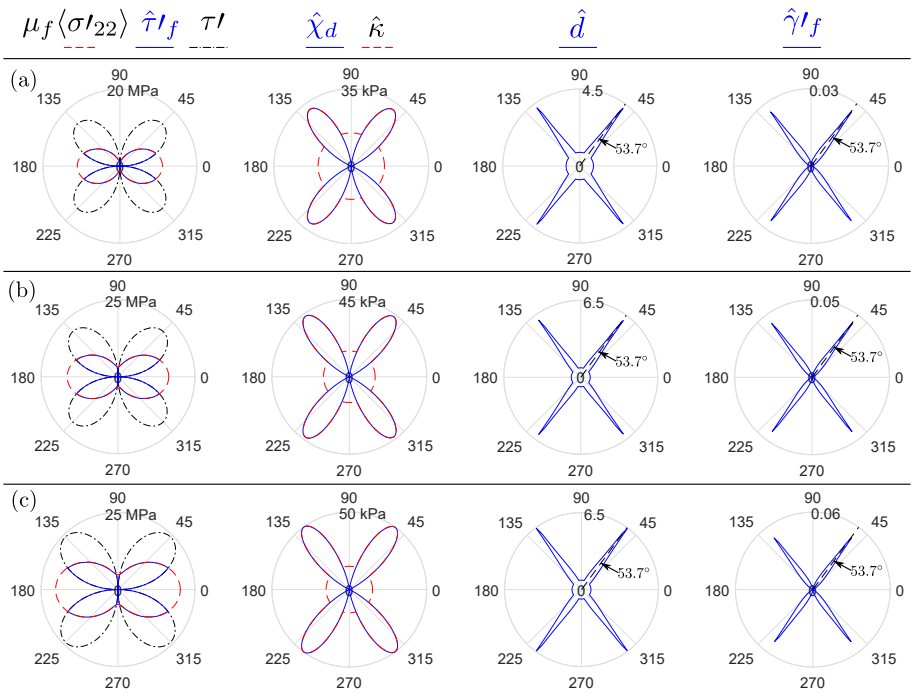

Figure 10. Plots of τ', $\hat{\tau}' f$, $\mu_f \langle \sigma' 22 \rangle$, $\hat{\chi}_d$, $\hat{\kappa}$, $\hat{d}$, and $\hat{\gamma}' f$ at the end of simulations for Red Wildmoor sandstone: (a) $\sigma_0 = 3.5MPa$, (b) $\sigma_0 = 10MPa$, (c) $\sigma_0 = 15MPa$.

Prepared using sagej.cls

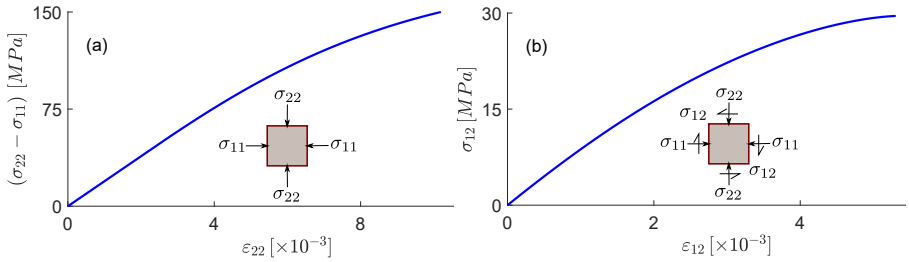

Figure 11. Predicted stress-strain response of intact Gosford sandstone: (a) biaxial loading, (b) simple shear loading.

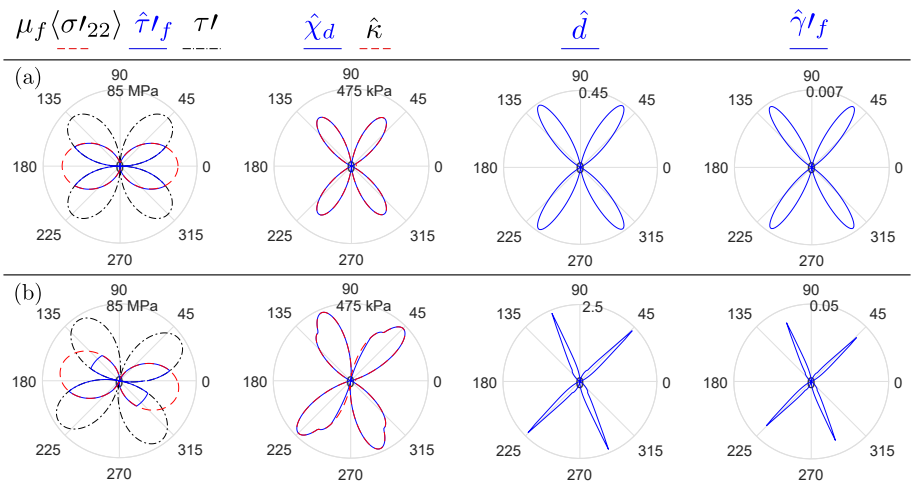

Figure 12. Plots of predicted $\tau\prime$, $\hat{\tau}\prime_f$, $\mu_f\langle\sigma\prime_{22}\rangle$, $\hat{\chi}_d$, $\hat{\kappa}$, $\hat{d}$, and $\hat{\gamma}\prime_f$ distribution for intact Gosford sandstone: (a) end of biaxial loading, (b) end of simple shear loading.